Electronic Supplementary Material (ESI) for Journal of Materials Chemistry A.

Supporting Information for

The role of phonons in switchable MOFs: A model material perspective

Alexander E. J. Hoffman,[a, †] Irena Senkovska,*[b, †] Leila Abylgazina,[b] Volodymyr Bon,[b] Veronika Grzimek,[c] Anna Maria Dominic,[d] Margarita Russina,[c] Marvin A. Kraft,[e] Inez Weidinger,[e] Wolfgang G. Zeier,[e] Veronique Van Speybroeck,*[a] Stefan Kaskel*[b]

1. *Samples characterization*

1.1 Samples overview

Table S1. Overview of the samples used in the study.

	XRD	N_2 physisorption isotherms	SEM	Crystal width range(mean), µm
Samples for inelastic neutron scattering				
Macro-sized crystals				
DUT-8(Ni)	Figure S1b,c	Figure S2a	Figure S3a	7 - 43 (17)
DUT-8(Co)	Figure S1b,c	Figure S2a	Figure S3b	9 - 25 (15)
DUT-8(Cu)	Figure S1a	Figure S2b	Figure S3c	4 - 19 (10)
Submicron-sized crystals				
DUT-8(Ni)	Figure S1a	Figure S2b	Figure S3d	0.04 - 0.08 (0.06)
DUT-8(Co)	Figure S1a	Figure S2b	Figure S3e	0.045 - 0.193 (0.106)
Samples for acoustic phonon spectroscopy				
Macro-sized crystals				
DUT-8(Ni)	Figure S4 a-c	-	Figure S5a	4 - 10 (7)
DUT-8(Co)	Figure S4 a-c	-	Figures S5b, S6a	18 - 104 (50)
DUT-8(Zn)	Figure S4 a-c	-	Figures S5c, S6b	82 - 243 (152)
Sample for raman spectroscopy				
Macro-sized crystals				
DUT-8(Cu)	Figure S7a	-	Figure S7b	9 - 44 (17)

1.2 Samples used for INS

a)

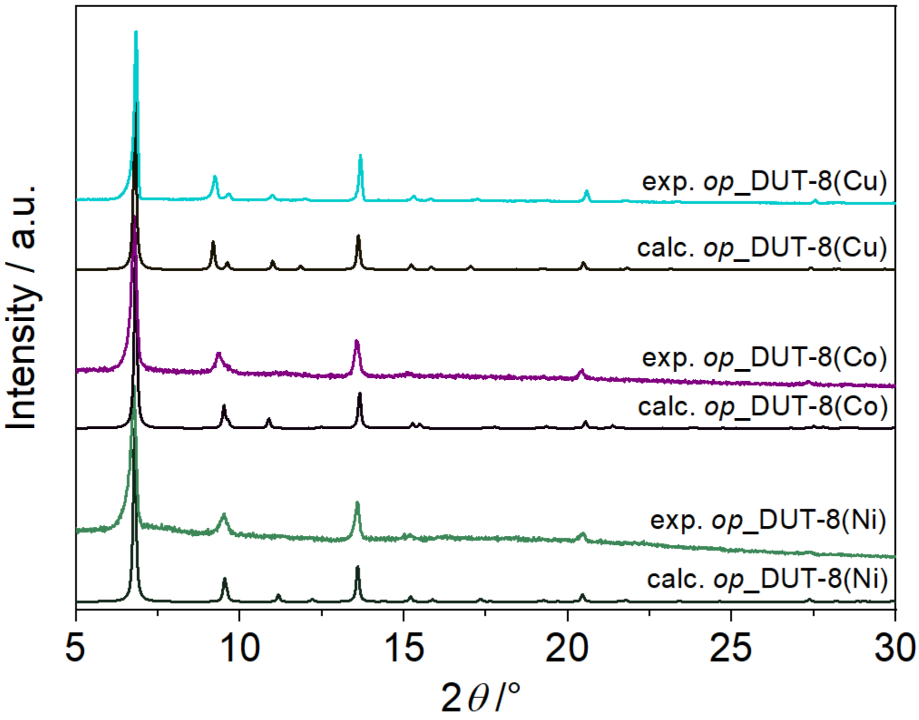

Figure S1: a) PXRD patterns of desolvated macro-sized DUT-8(Cu)_*op*, desolvated submicron-sized DUT-8(Co)_op and DUT-8(Ni)_op in comparison with patterns of DUT-8(M)_*op* phases calculated from the single crystal structures.

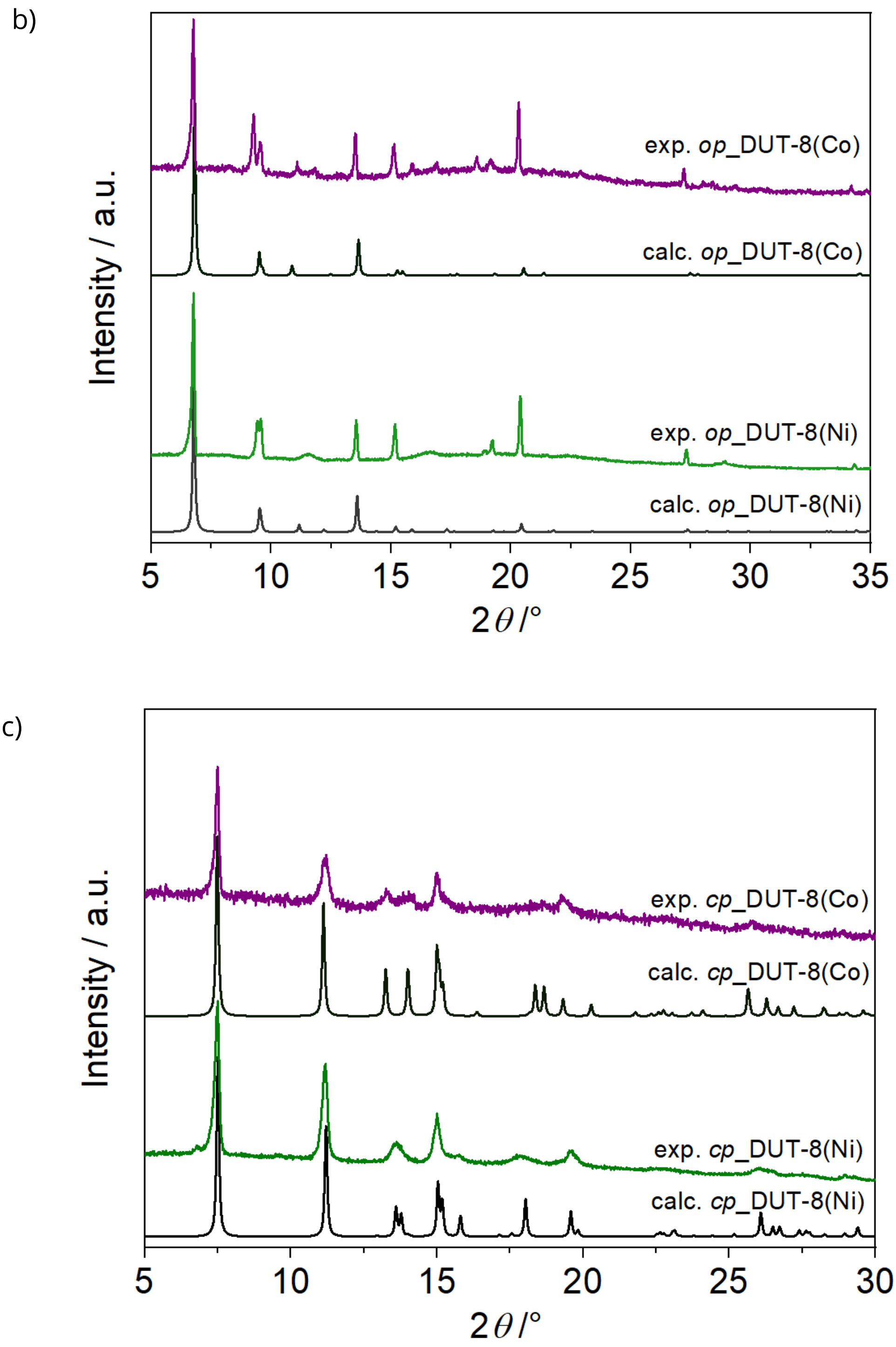

Figure S1: PXRD patterns of DUT-8(M), M = Ni, Co: b) solvated macro-sized samples (*op*) and c) desolvated macro-sized samples (*cp*) in comparison with patterns calculated from the DUT-8(M) crystal structures.

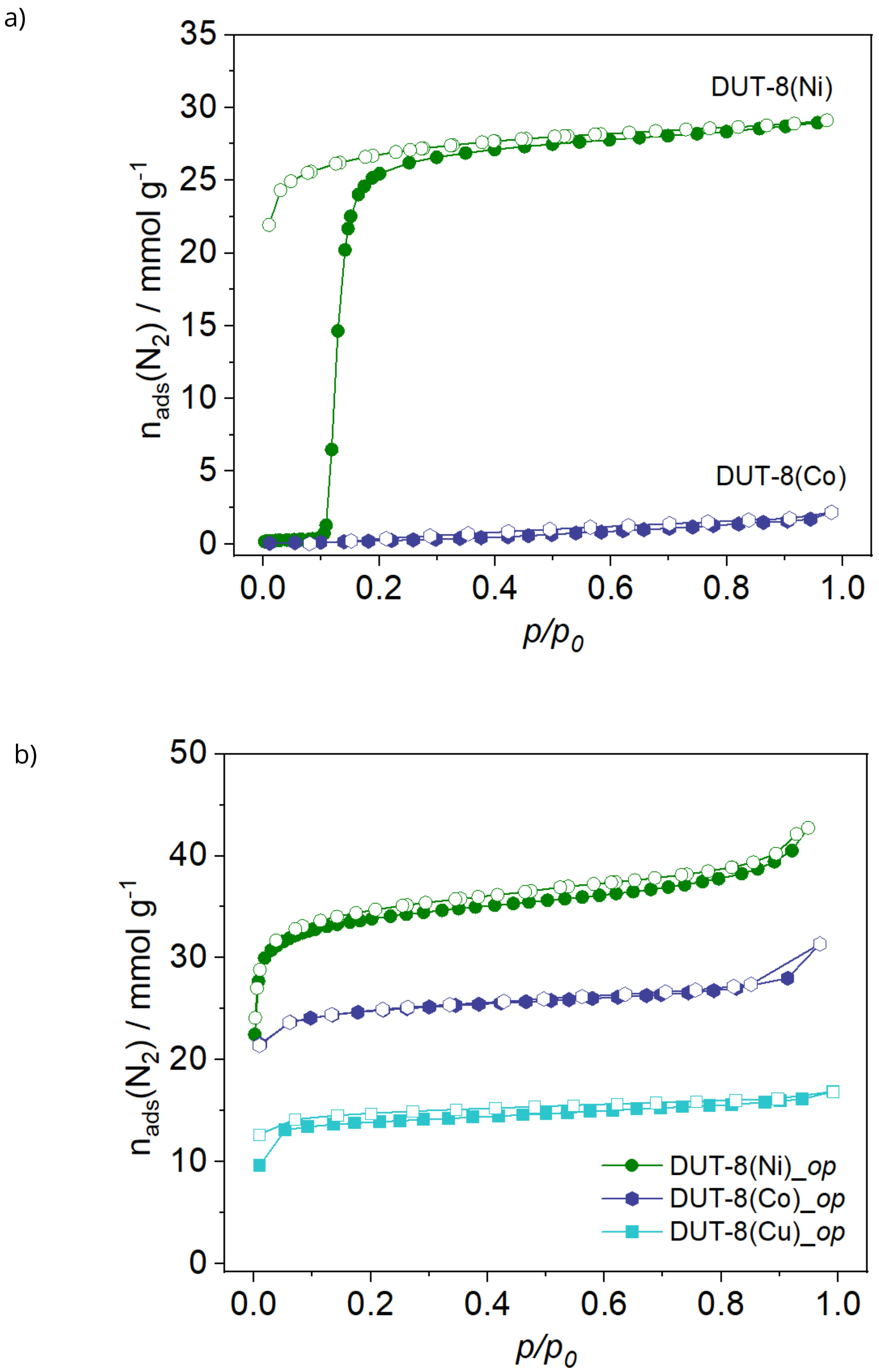

Figure S2: Nitrogen adsorption isotherms of a) DUT-8(M)_*cp* and b) DUT-8(M)_*op* samples. *M* = Ni, Co, Cu.

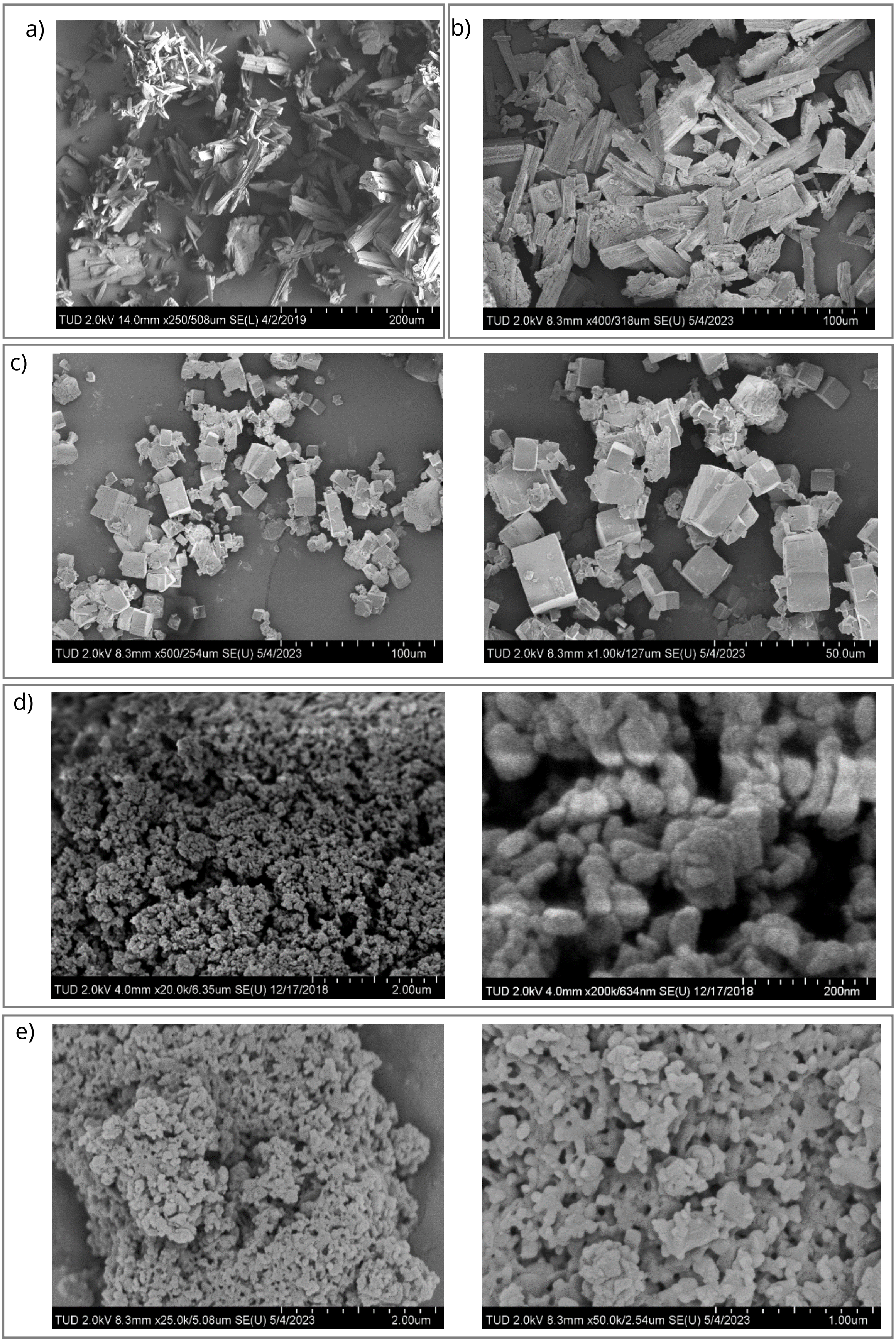

Figure S3: SEM images of desolvated macro-sized crystals: a) DUT-8(Ni); b) DUT-8(Co); c) DUT-8(Cu); and submicron-sized crystals: d) DUT-8(Ni); e) DUT-8(Co).

1.2 Samples used for phonon acoustic spectroscopy

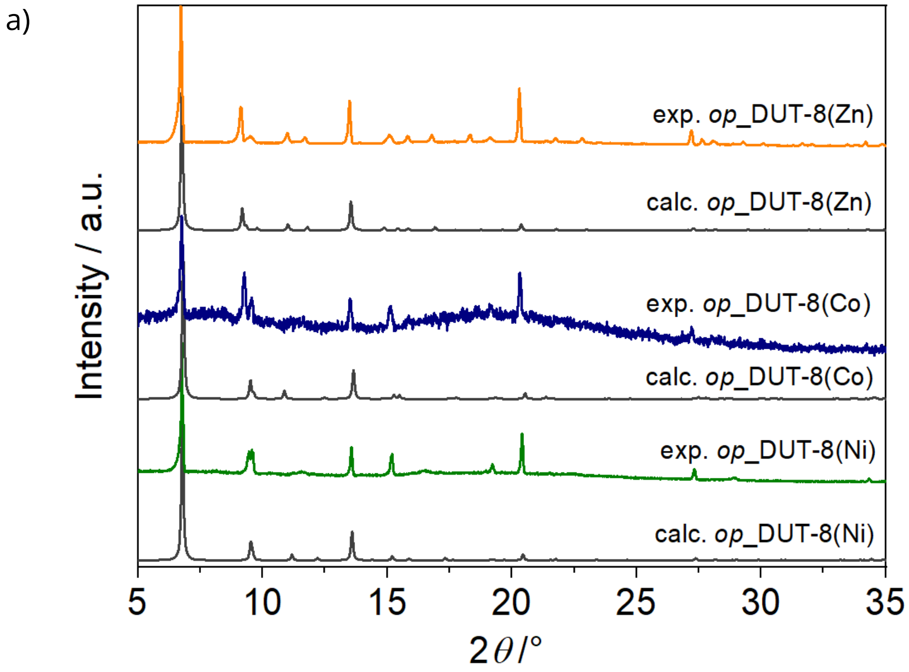

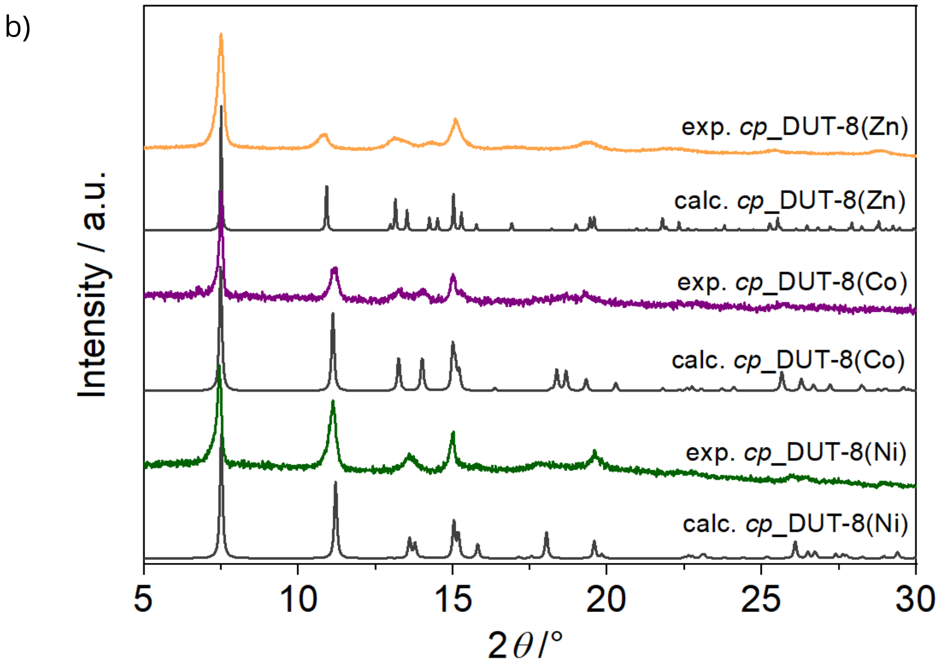

c)

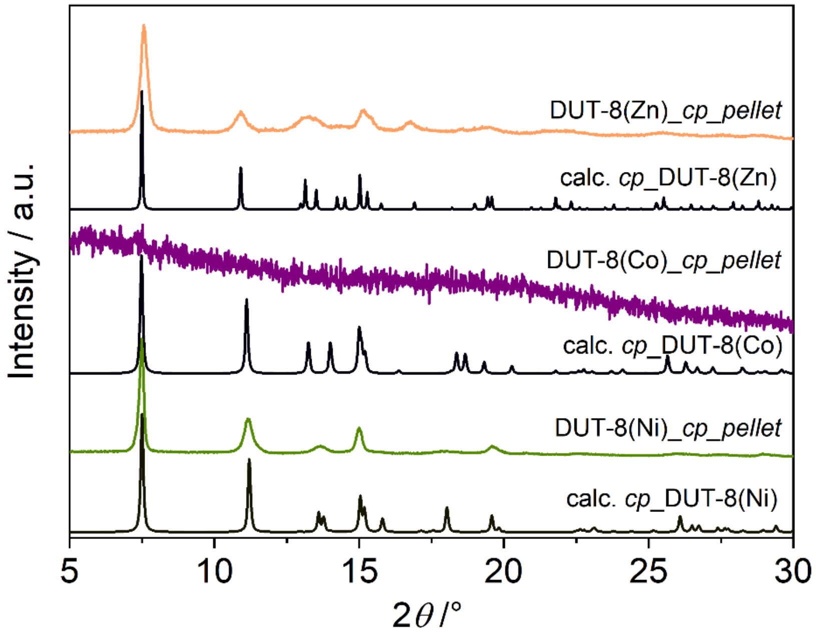

Figure S4: PXRD patterns of the macro-sized DUT-8(M) (M = Ni, Co, Zn) crystals: a) solvated in DMF (*op*); b) desolvated (*cp*); c) pelletised for phonon acoustic spectroscopy.

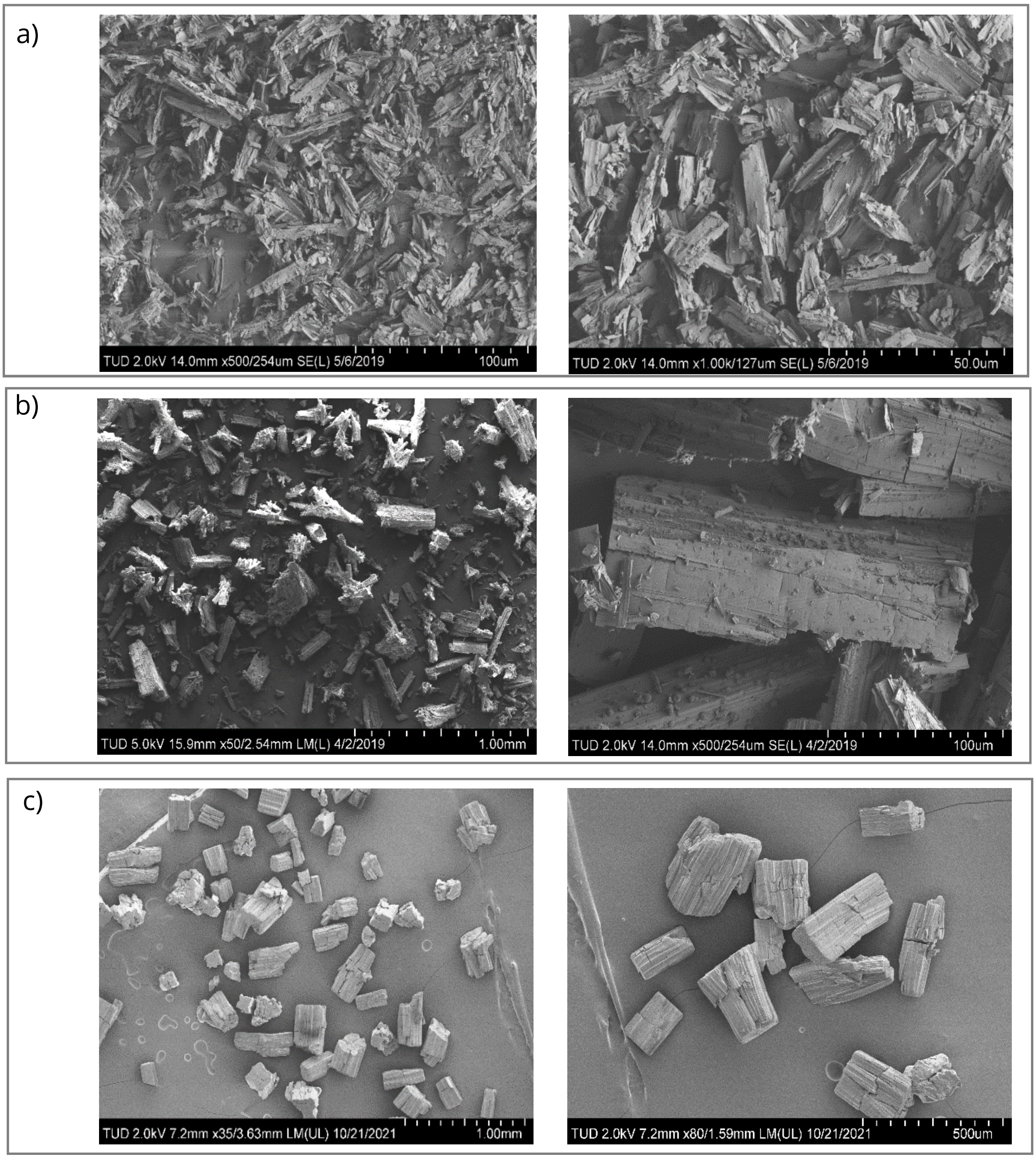

Figure S5: SEM images of desolvated macro-sized crystals: a) DUT-8(Ni); b) DUT-8(Co); c) DUT-8(Zn).

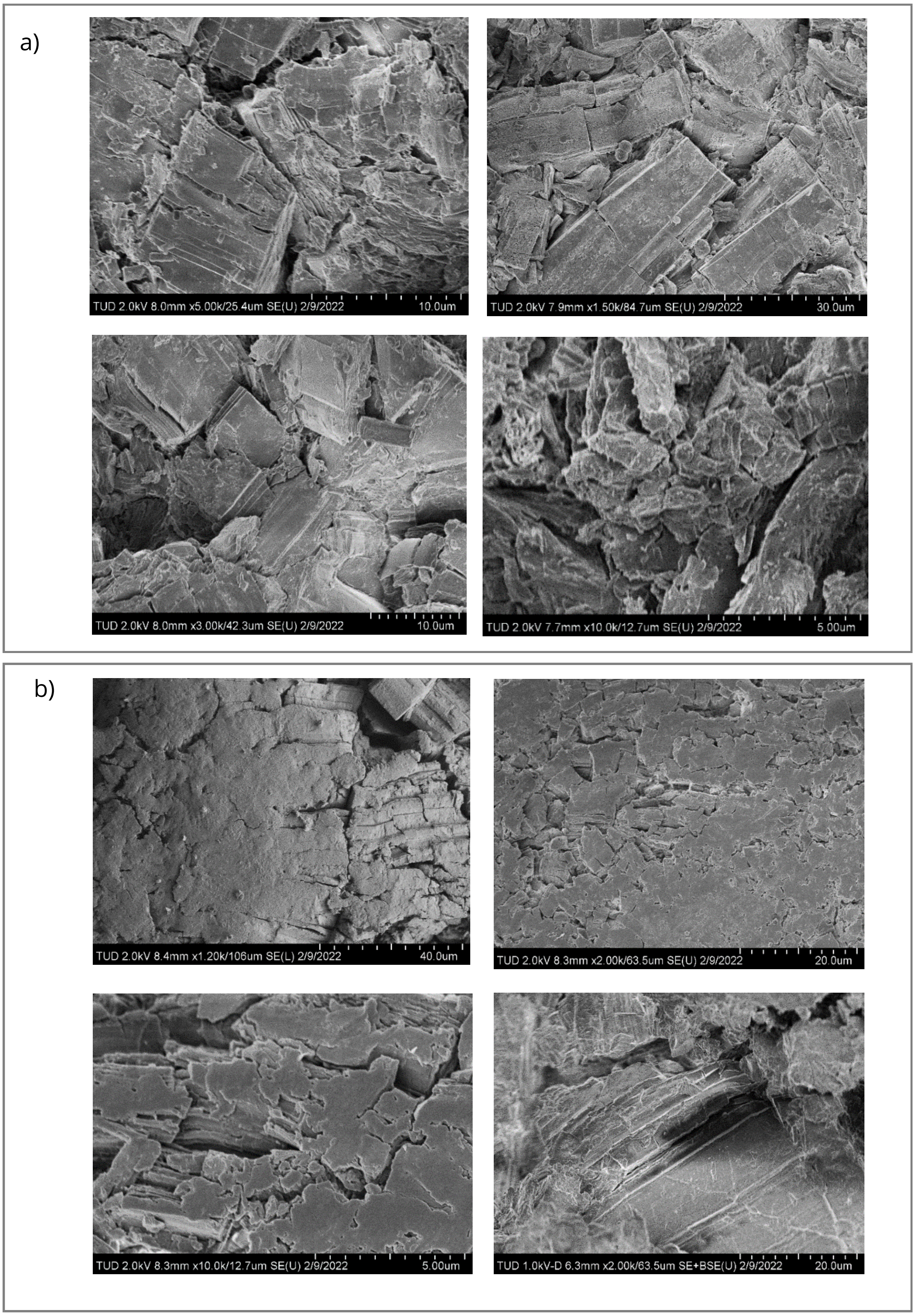

Figure S6: SEM images of a) DUT-8(Co) pellet, b) DUT-8(Zn) pellet.

1.3 Sample used for Raman spectroscopy

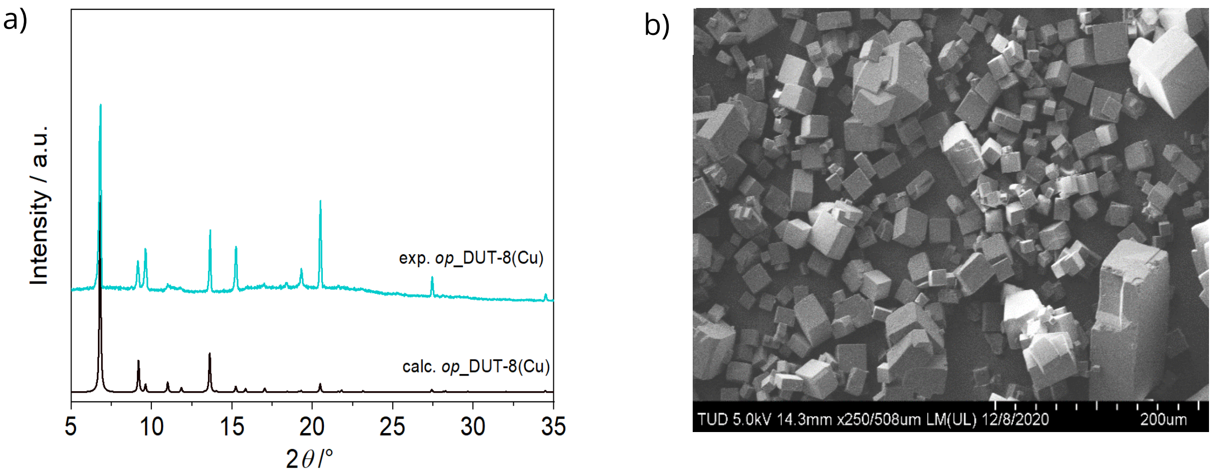

Figure S7: a) PXRD pattern of solvated macro-sized crystals (op) of DUT-8(Cu) in comparison with pattern calculated from the DUT-8(Cu) single crystal structure; b) SEM image of DUT-8(Cu).

2. Optimised structural parameters from static DFT calculations

2.1. Open pore phases

Table S2: Experimental crystallographic data for DUT-8(M)_*op* phases solvated with DMF crystallising in *C*2/*m* space group* and structural parameters of the theoretically optimised DUT-8(M) materials in the solvent-free op state.

	Experiment DUT-8(Ni) CCDC 1912198	Theory DUT-8(Ni)	Experiment DUT-8(Co) CCDC 1912199	Theory DUT-8(Co)	Experiment DUT-8(Zn) CCDC 2020029	Theory DUT-8(Zn)	Experiment DUT-8(Cu) CCDC 2189425	Theory DUT-8(Cu)
Unit cell parameters / Å, °	*a*=18.470 *b*=18.390 *c*=9.311 *ß*=98.72	*a* = 18.40 *b* = 18.83 *c* = 9.24 *α* = 90.91 *ß* = 103.41 *γ* = 90.02	*a*=18.720 *b*=18.340 *c*=9.490 *ß* = 101.77	*a* = 18.71 *b* = 18.68 *c* = 9.43 *α* = 90.96 *ß* = 99.27 *γ* = 89.98	*a*=19.000 *b*=18.070 *c*=9.670 *ß*=95.87	*a* = 18.76 *b* = 18.59 *c* = 9.56 *α* = 90.73 *ß* = 99.26 *γ* = 90.01	*a*=18.510 *b*=18.370 *c*=9.680 *ß*=96.31	*a* = 18.67 *b* = 18.41 *c* = 9.64 *α* = 90.43 *ß* = 98.48 *γ* = 89.97
Cell volume/ Å^3	3125	3113	3190	3251	3303	3290	3272	3277
M…M distance/ Å	2.653	2.49	2.691	2.26	2.966	2.80	2.678	2.55
M–N bond length/ Å	2.042	2.11	2.111	2.29	2.084	2.10	2.231	2.26
M–M–N angle/ °	177.6	166	171.8	175	178.7	177	178.9	178

* The unit cell of the *op* phase contains 4 metal atoms, four 2,6-ndc and two dabco molecules.

2.2. Closed pore phases

Table S3: Crystallographic data for DUT-8(M)_cp* crystallising in *P*1 space group and structural parameters of the theoretically optimised DUT-8(M) materials in the cp phase.

	Experiment DUT-8(Ni) 1034317	Theory DUT-8(Ni)	Experiment DUT-8(Co) 1912233	Theory DUT-8(Co)	Experiment DUT-8(Zn) 2020030	Theory DUT-8(Zn)	Theory DUT-8(Cu)
Cell parameters / Å, °	*a* = 6.947 *b* = 8.181 *c* = 12.172 *α* = 91.141 *β* = 103.87 *γ* = 104.55	*a* = 6.84 *b* = 23.89 *c* = 9.22 *α* = 90.10 *ß* = 122.59 *γ* = 90.83	*a* = 7.045 *b* = 8.298 *c* = 12.140 *α* = 81.24 *β* = 102.22 *γ* = 105.56	*a* = 6.89 *b* = 23.92 *c* = 9.36 *α* = 88.87 *ß* = 123.92 *γ* = 92.60	*a* = 7.1279 *b* = 8.5505 *c* = 13.1270 *α* = 84.1477 *β* = 116.0322 *γ* = 108.4626	*a* = 6.92 *b* = 23.80 *c* = 9.57 *α* = 89.49 *ß* = 123.44 *γ* = 95.53	*a* = 6.89 *b* = 23.75 *c* = 9.54 *α* = 90.61 *ß* = 123.91 *γ* = 93.16
Cell volume/ Å^3	648	1270	665	1279	681	1306	1292
M…M distance/ Å	2.736	2.59	2.636	2.48	3.80	2.97	2.63
M–N bond length/ Å	1.906 2.086	2.09	2.15(9) 2.13(9)	2.19	2.293 2.098	2.08	2.13 2.24
M–M–N angle/ °	153.93	158	141.50	162	117.31	160	168

* The unit cell of the *cp* phase contains two metal atom, two 2,6-ndc and one dabco molecule. For the theoretical calculations, the unit cell is doubled compared to the experimental unit cell to have consistent calculations between cp and op phases.

3. Visualisation of experimental and theoretically optimised crystal structures

3.1. Open pore phases of DUT-8(M)

3.1.1. DUT-8(Ni)

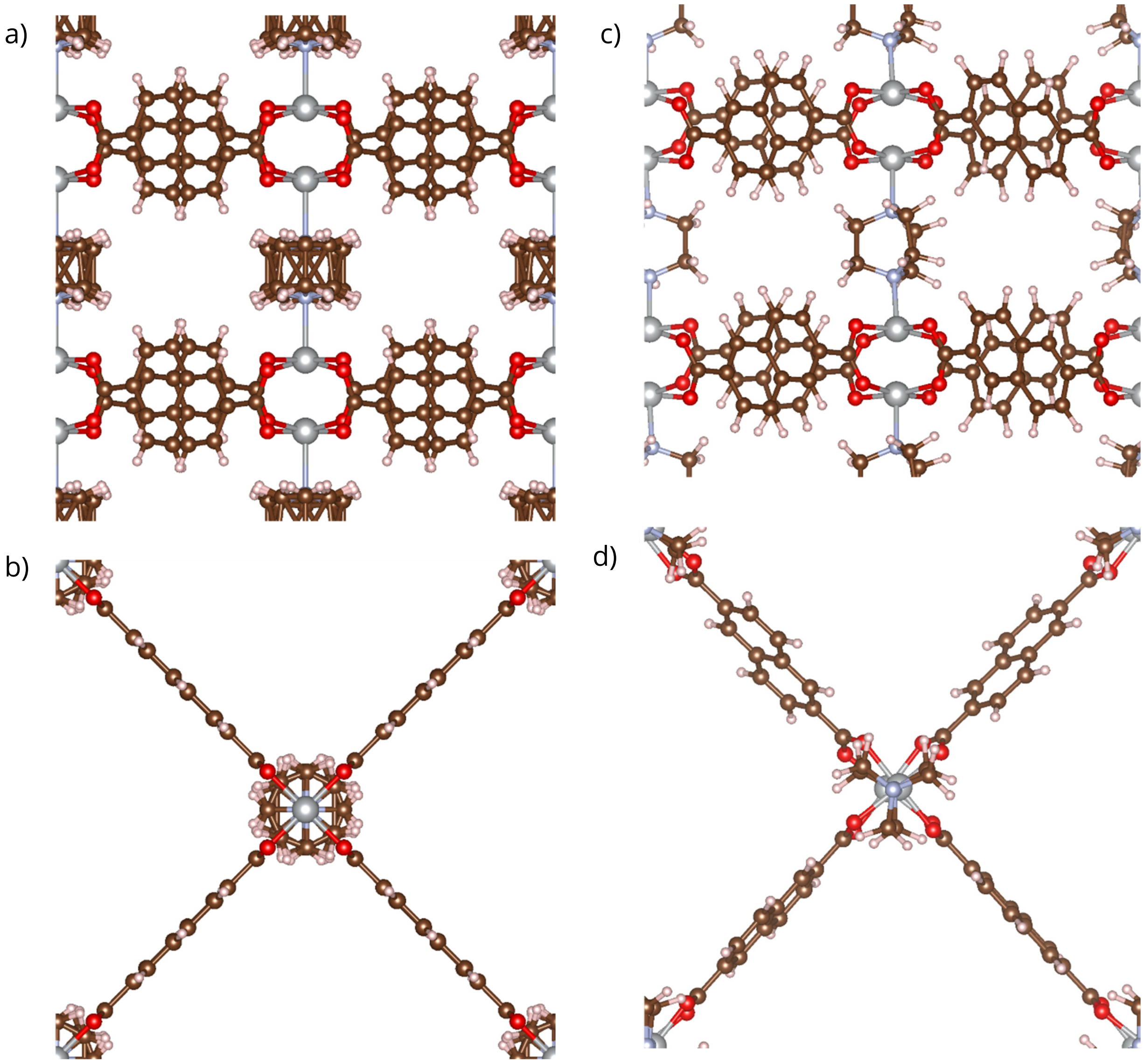

Figure S8: Visualisation of the experimental (a, b) and theoretically optimised (c, d) op phase structure of DUT-8(Ni). (a, c) View on the 1D chain with dabco pillars and paddle wheel unit and the linker stacking. (b, d) View along the pore channel.

3.1.2. DUT-8(Co)

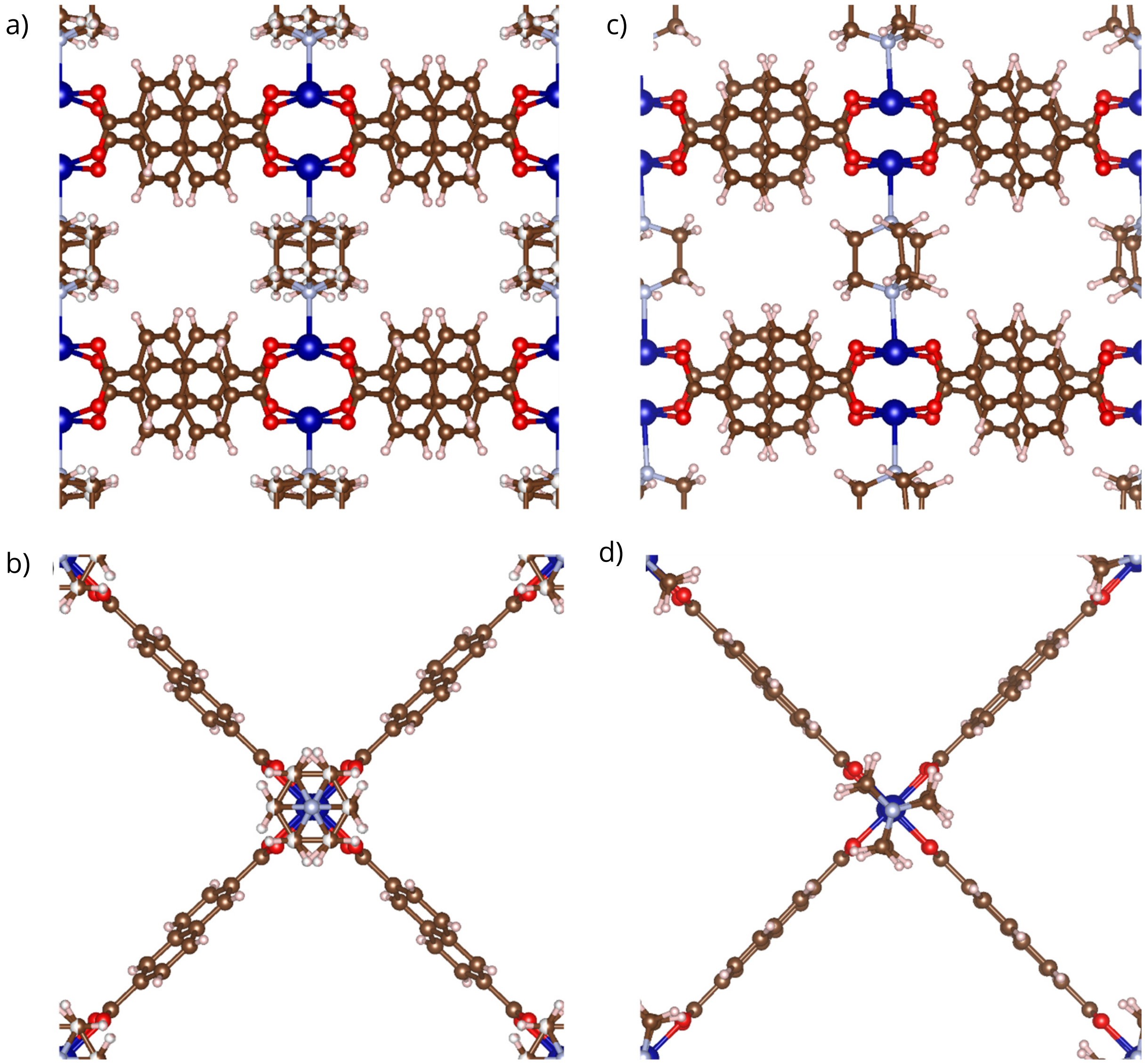

Figure S9: Visualisation of the experimental (a, b) and theoretically optimised (c, d) op phase structure of DUT-8(Co). (a, c) View on the 1D chain with dabco pillars and paddle wheel unit and the linker stacking. (b, d) View along the pore channel.

3.1.3. DUT-8(Zn)

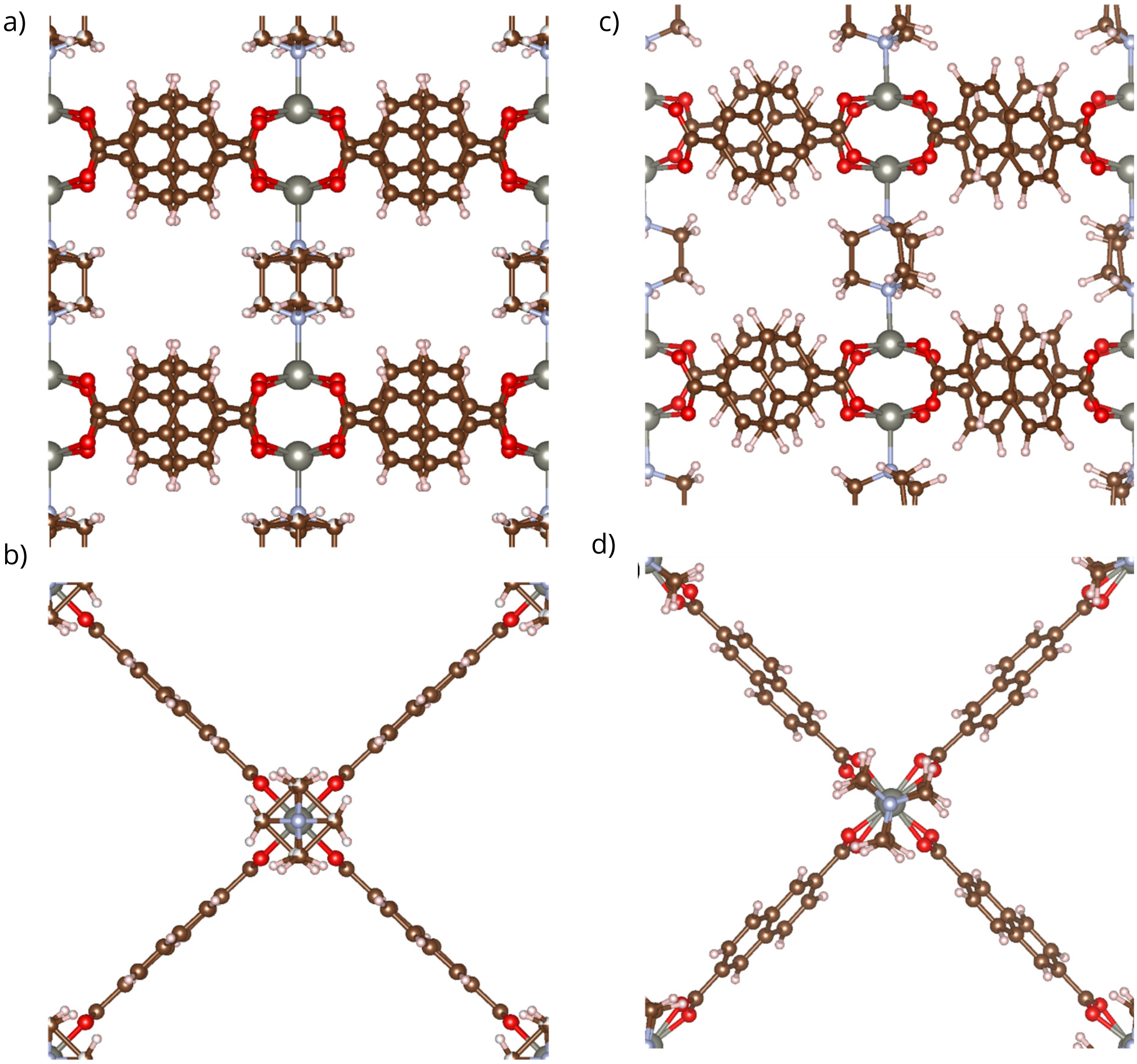

Figure S10: Visualisation of the experimental (a, b) and theoretically optimised (c, d) op phase structure of DUT-8(Zn). (a, c) View on the 1D chain with dabco pillars and paddle wheel unit and the linker stacking. (b, d) View along the pore channel.

3.1.4. DUT-8(Cu)

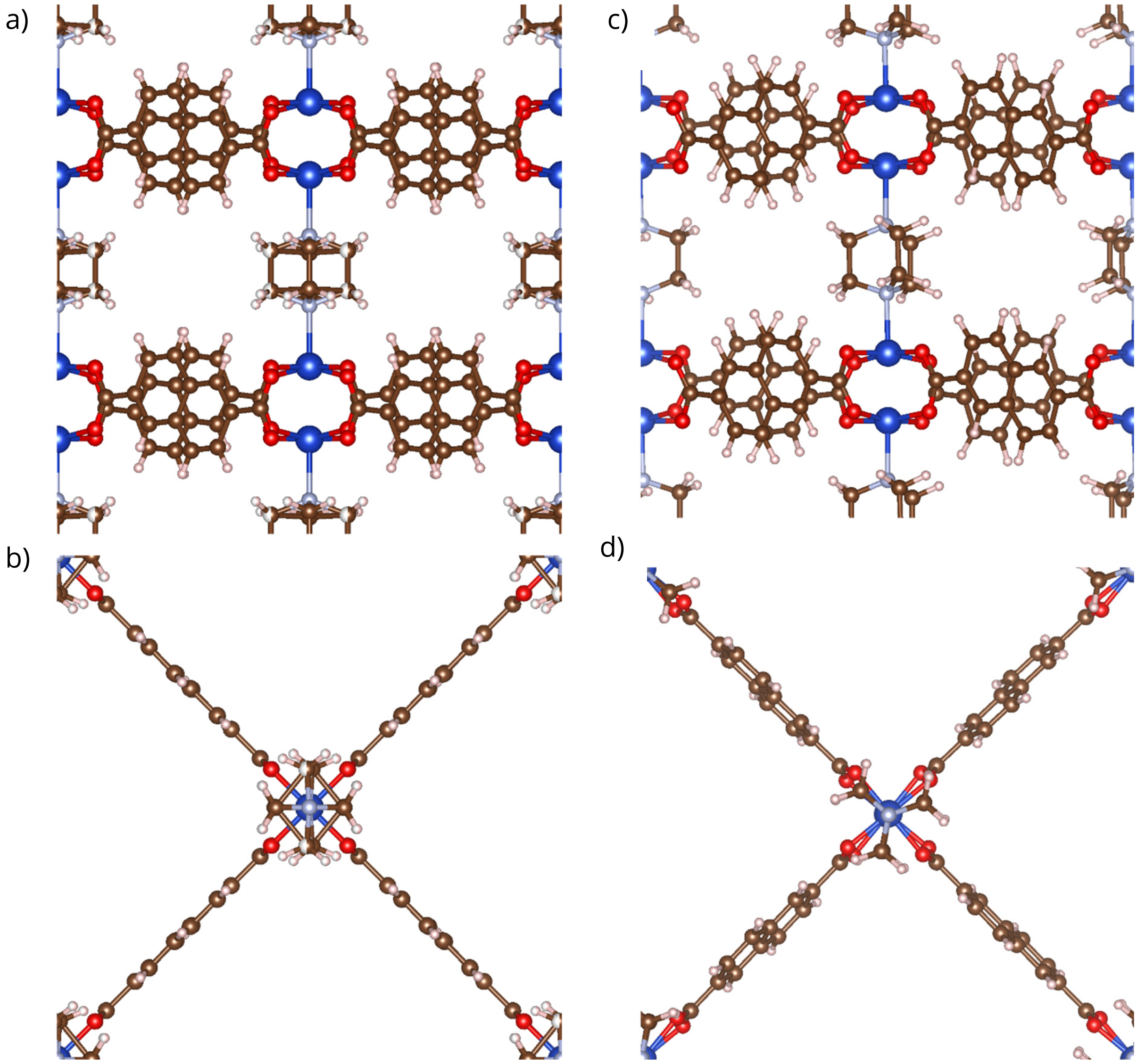

Figure S11: Visualisation of the experimental (a, b) and theoretically optimised (c, d) *op* phase structure of DUT-8(Cu). (a, c) View on the 1D chain with dabco pillars and paddle wheel unit and the linker stacking. (b, d) View along the pore channel.

3.2. Closed pore phases of DUT-8(M)

3.2.1. DUT-8(Ni)

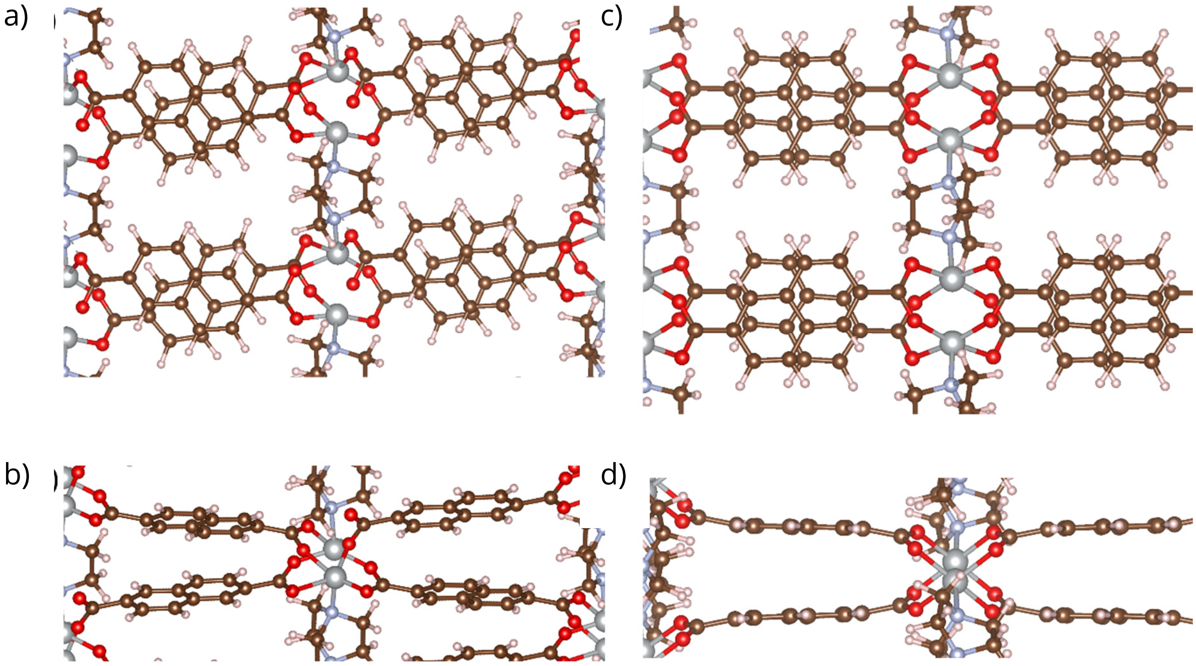

Figure S12: Visualisation of the experimental (a, b) and theoretically optimised (c, d) *cp* phase structure of DUT-8(Ni). (a, c) View on the 1D chain with dabco pillars and paddle wheel unit and the linker stacking. (b, d) View *along* the pore channel.

3.2.2. DUT-8(Co)

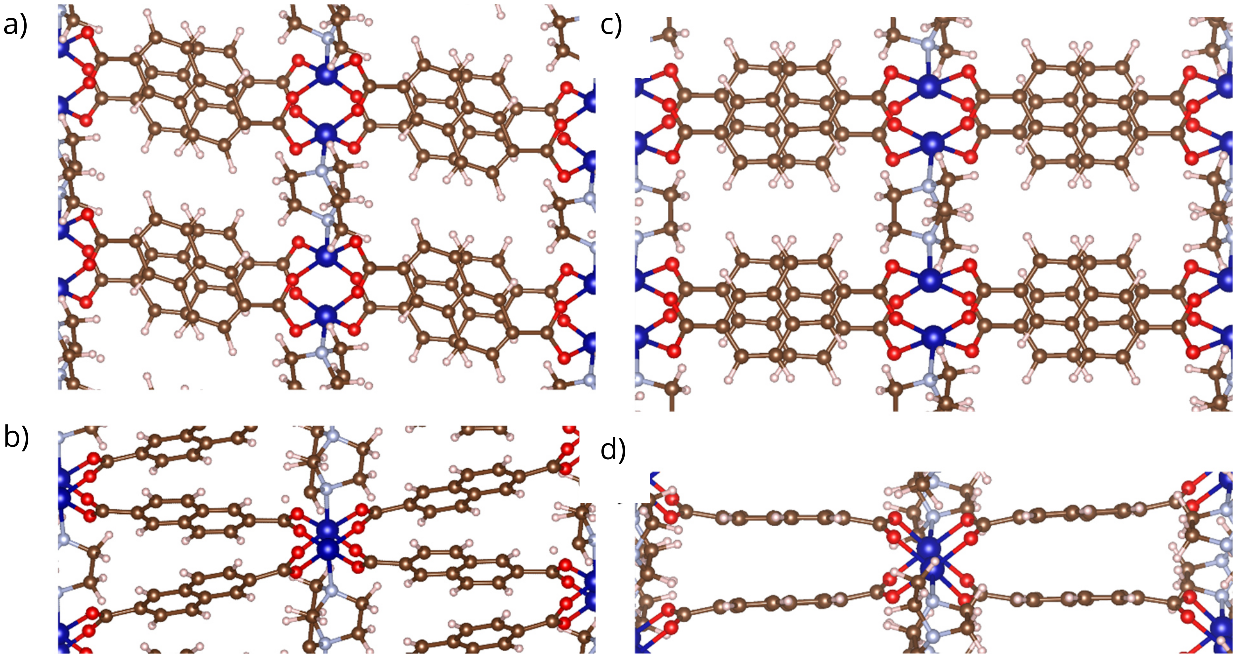

Figure S13: Visualisation of the experimental (a, b) and theoretically optimised (c, d) *cp* phase structure of DUT-8(Co). (a, c) View on the 1D chain with dabco pillars and paddle wheel unit and the linker stacking. (b, d) View *along* the pore channel.

3.2.3. DUT-8(Zn)

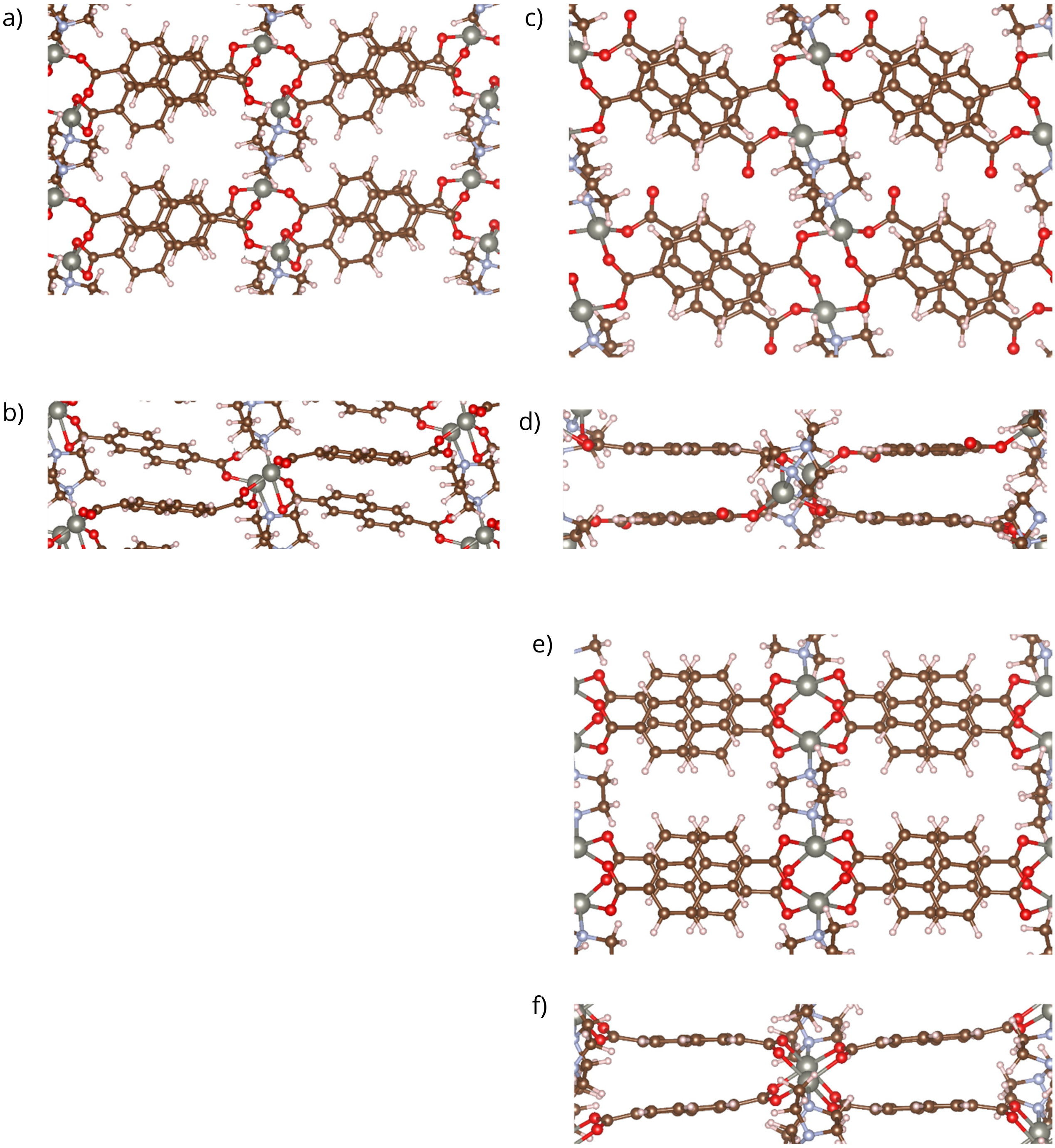

Figure S14: Visualisation of the experimental (a, b) and theoretically optimised (c - f) *cp* phase structure of DUT-8(Zn). (a, c) View on the 1D chain with dabco pillars and paddle wheel unit and the linker stacking. (b, d) View *along* the pore channel. (e, f) Optimised structure with intact paddle wheels.

4. Visualisation of terahertz vibrations in DUT-8(Zn)

4.1. Open pore phase

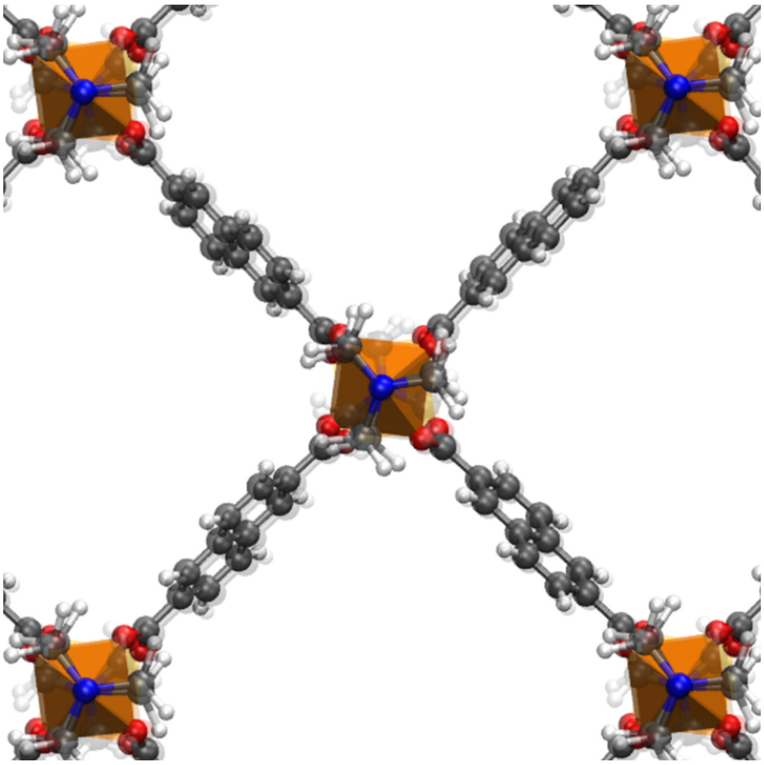

Figure S15: Terahertz vibration at 7 cm^{-1} in the op phase structure of DUT-8(Zn) inducing rotations of the dabco pillars.

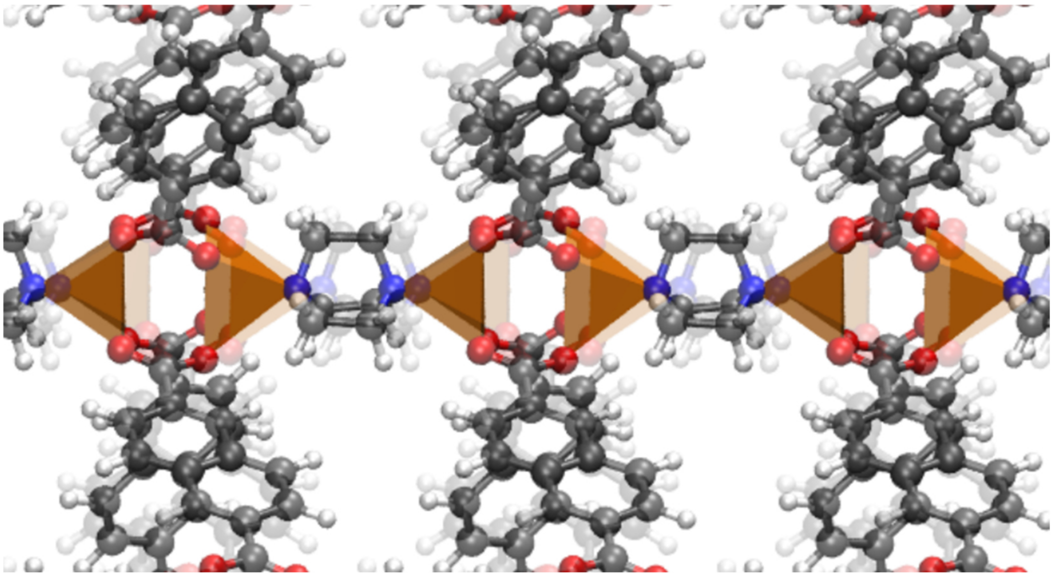

Figure S16: Terahertz vibration at 15 cm^{-1} in the op phase structure of DUT-8(Zn) inducing translations of the paddle wheel units and the dabco pillars together with rotational movement of the 2,6-ndc linker.

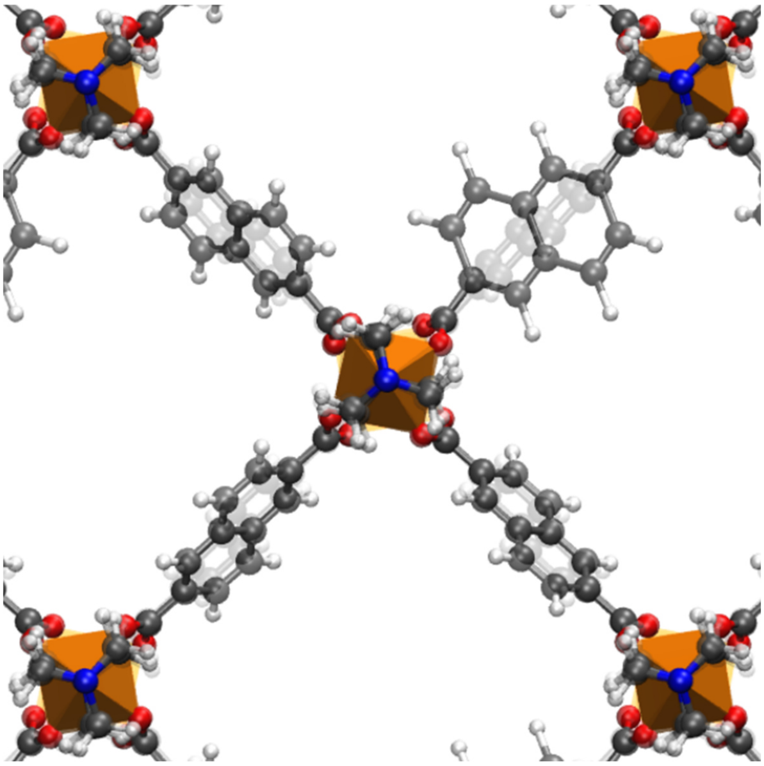

Figure S17: Terahertz vibration at 21 cm^{-1} in the op phase structure of DUT-8(Zn) inducing rotations of the 2,6-ndc linkers.

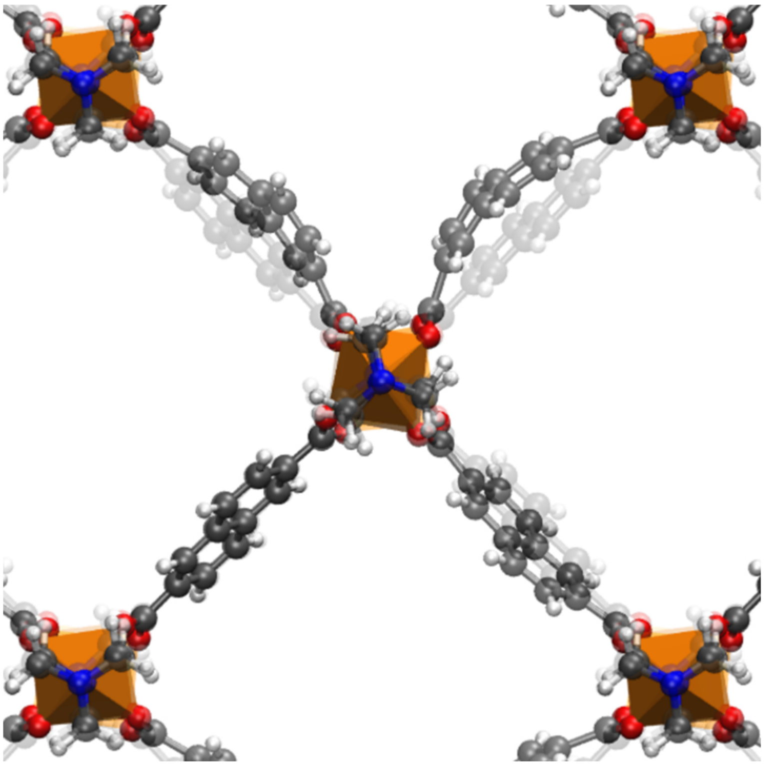

Figure S18: Terahertz vibration at 34 cm^{-1} in the op phase structure of DUT-8(Zn) inducing translations of the 2,6-ndc linkers (trampoline motion).

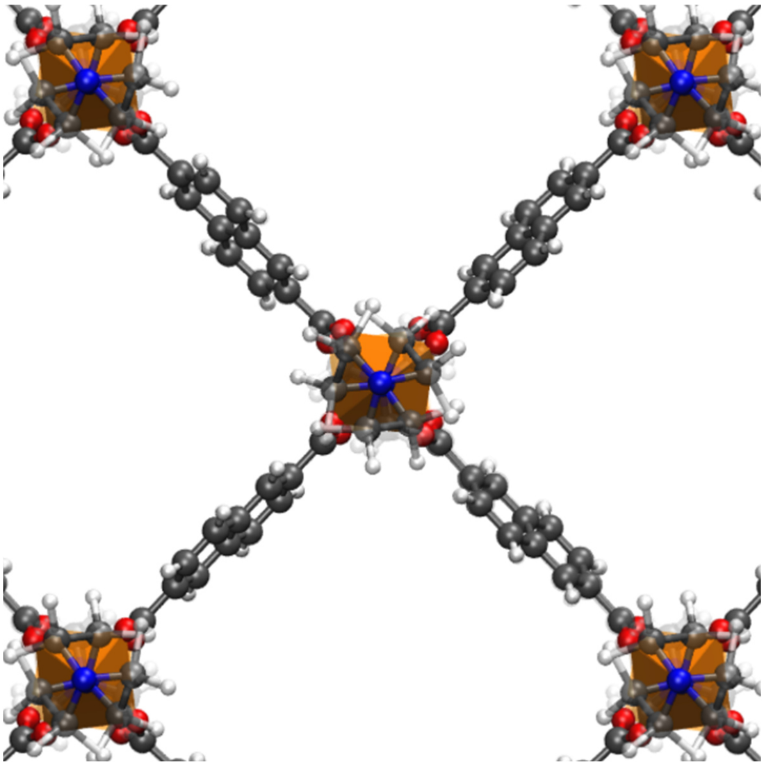

Figure S19: Terahertz vibration at 72 cm^{-1} in the op phase structure of DUT-8(Zn) inducing distortions of the dabco pillars.

4.2. Closed pore phases

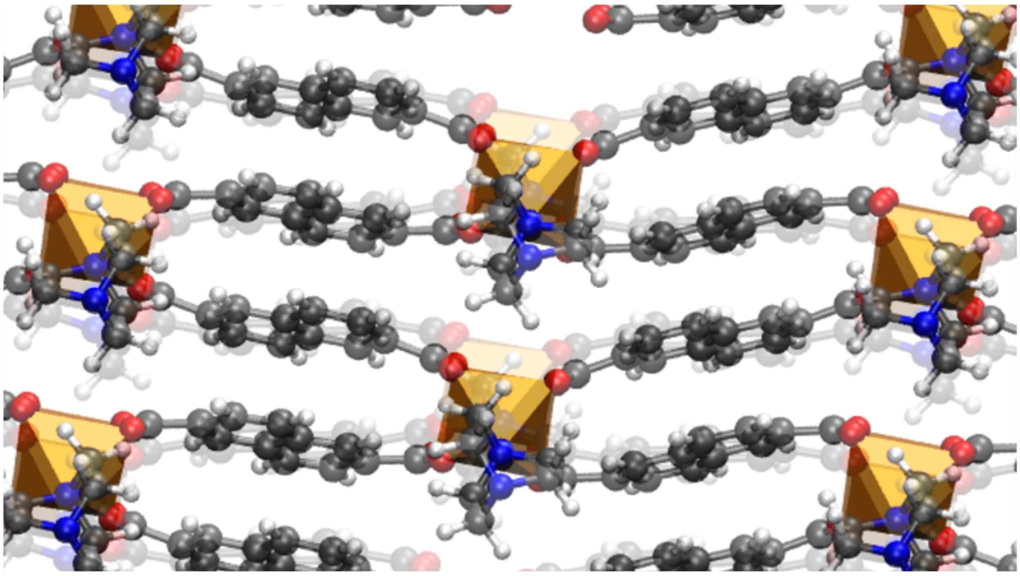

Figure S20: Terahertz vibration at 16 cm^{-1} in the cp phase structure of DUT-8(Zn) inducing translations of the paddle wheel units and the dabco pillars together with a slight tilting of the 2,6-ndc linkers.

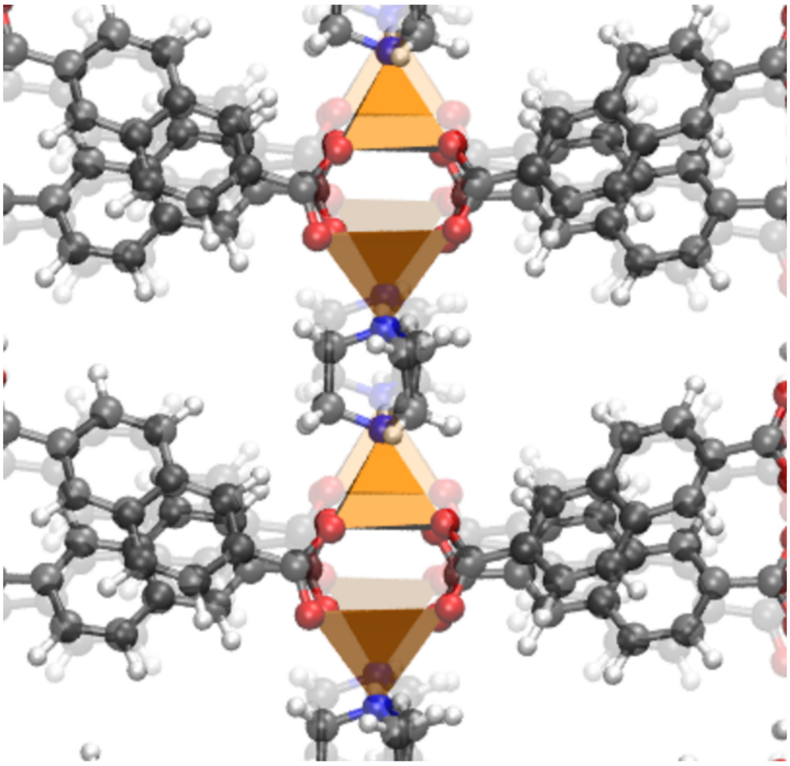

Figure S21: Terahertz vibration at 32 cm^{-1} in the cp phase structure of DUT-8(Zn) inducing translations of the paddle wheel units and the dabco pillars together with a slight tilting of the 2,6-ndc linkers.

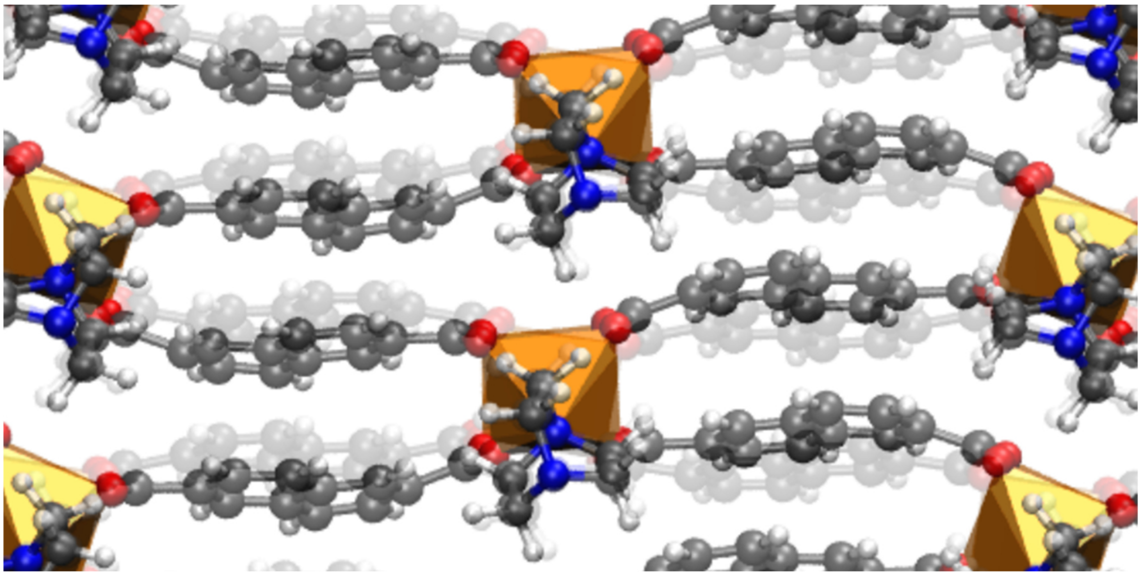

Figure S22: Terahertz vibration at 25 cm^{-1} in the cp phase structure of DUT-8(Zn) inducing rotations of the paddle wheel units together with translations of the 2,6-ndc linkers.

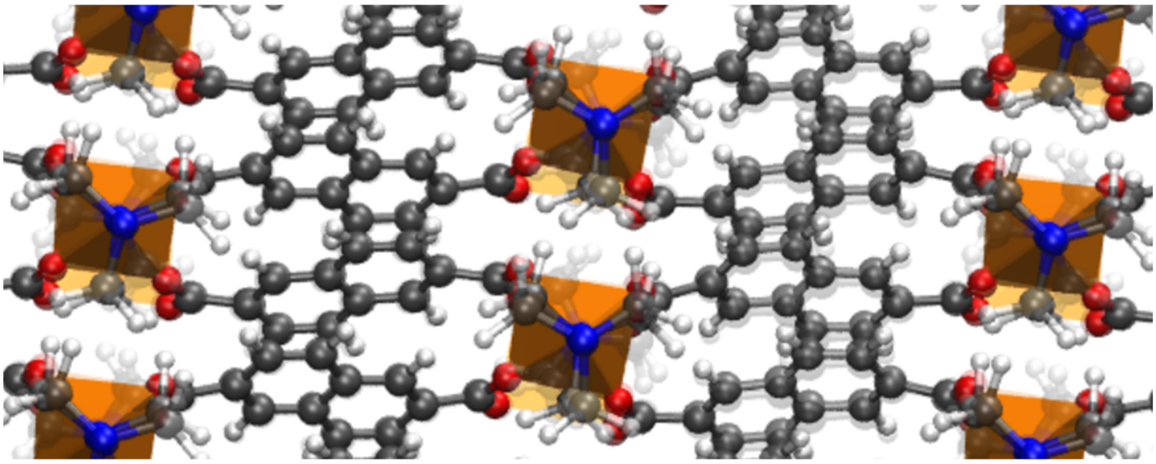

Figure S23: Terahertz vibration at 37 cm^{-1} in the cp phase structure of DUT-8(Zn) inducing rotations of the dabco pillars.

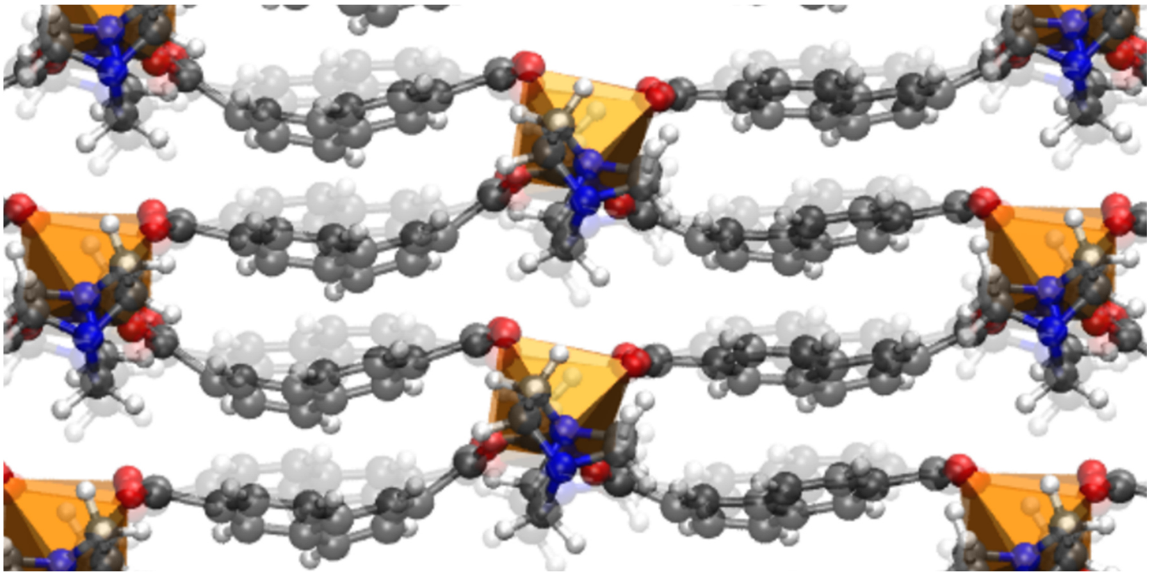

Figure S24: Terahertz vibration at 47 cm^{-1} in the cp phase structure of DUT-8(Zn) inducing translations of the 2,6-ndc linkers with slight translations of the paddle wheel units and dabco pillars.

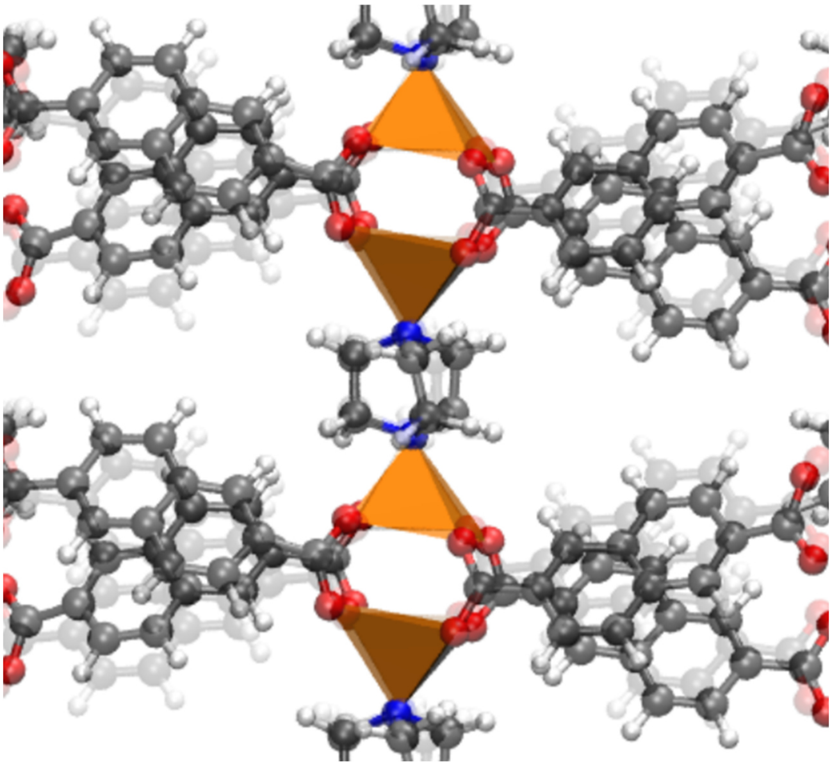

Figure S25: Terahertz vibration at 51 cm^{-1} in the cp phase structure of DUT-8(Zn) inducing translations of the 2,6-ndc linkers with slight rotations of the paddle wheel units.

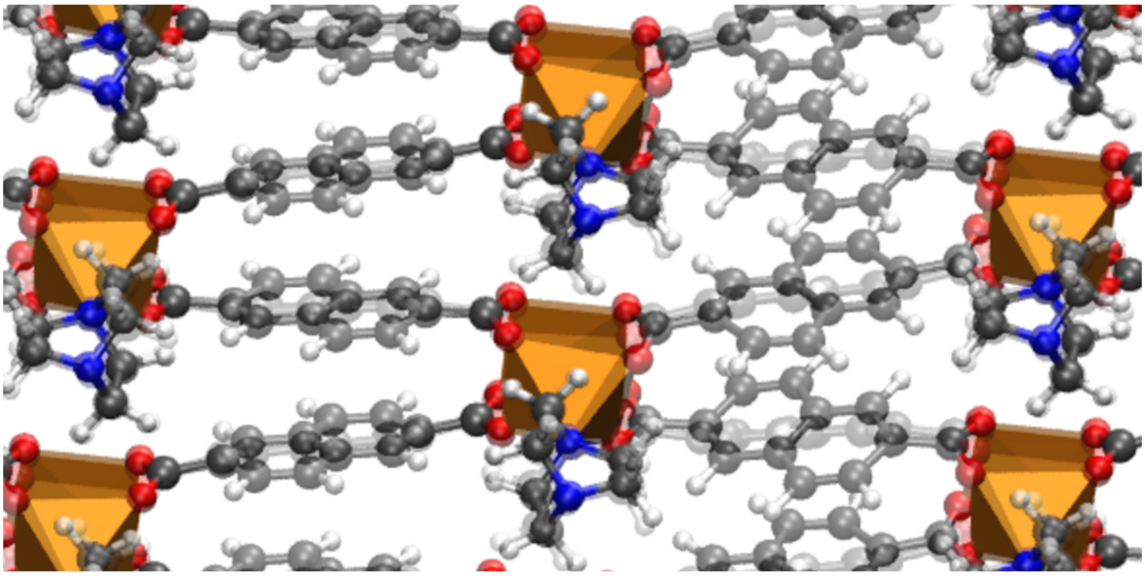

Figure S26: Terahertz vibration at 59 cm^{-1} in the cp phase structure of DUT-8(Zn) inducing translations of the paddle wheel unit and the dabco pillars together with a slight tilting of the 2,6-ndc linkers.

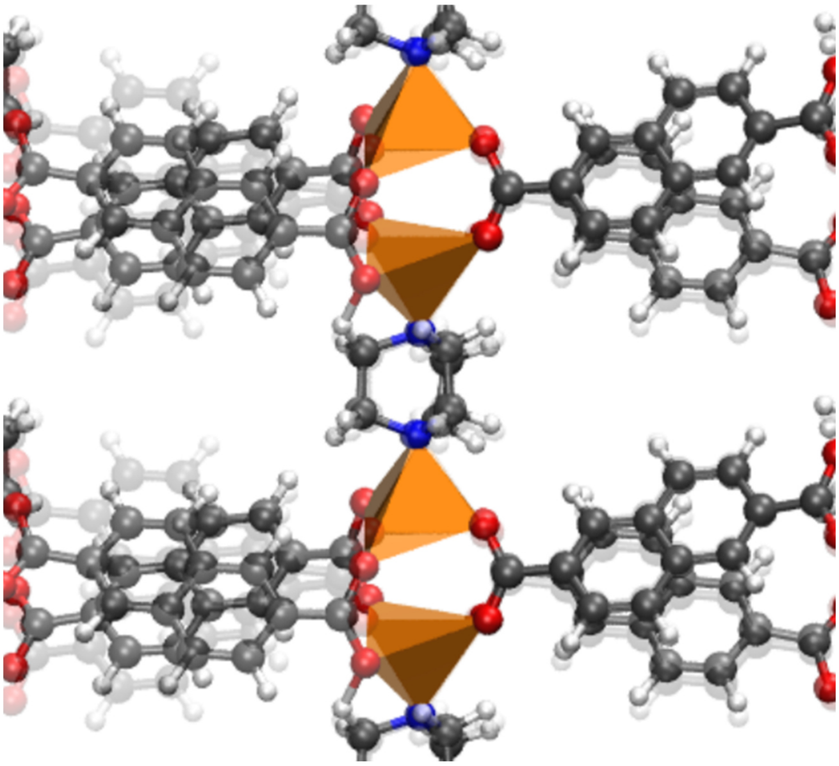

Figure S27: Terahertz vibration at 60 cm^{-1} in the cp phase structure of DUT-8(Zn) inducing translations of the 2,6-ndc linkers with slight rotations of the paddle wheel units.

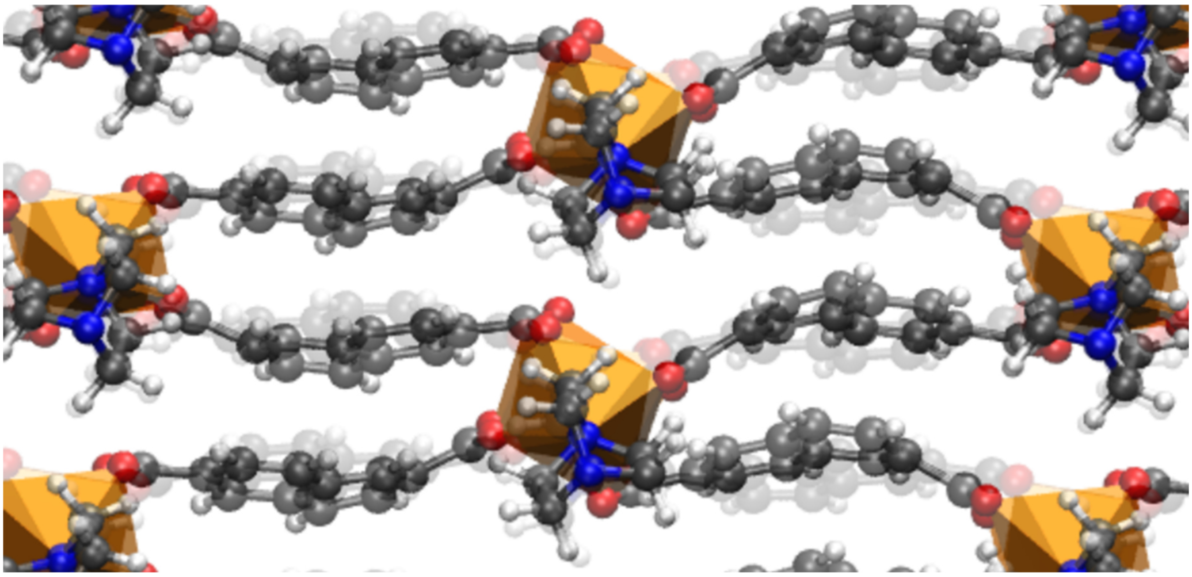

Figure S28: Terahertz vibration at 71 cm^{-1} in the cp phase structure of DUT-8(Zn) inducing translations of the 2,6-ndc linkers with slight rotations of the paddle wheel units.

5. Mode character for terahertz vibrations in DUT-8(M) (M = Ni, Co, Zn, Cu)

5.1. Open pore phases

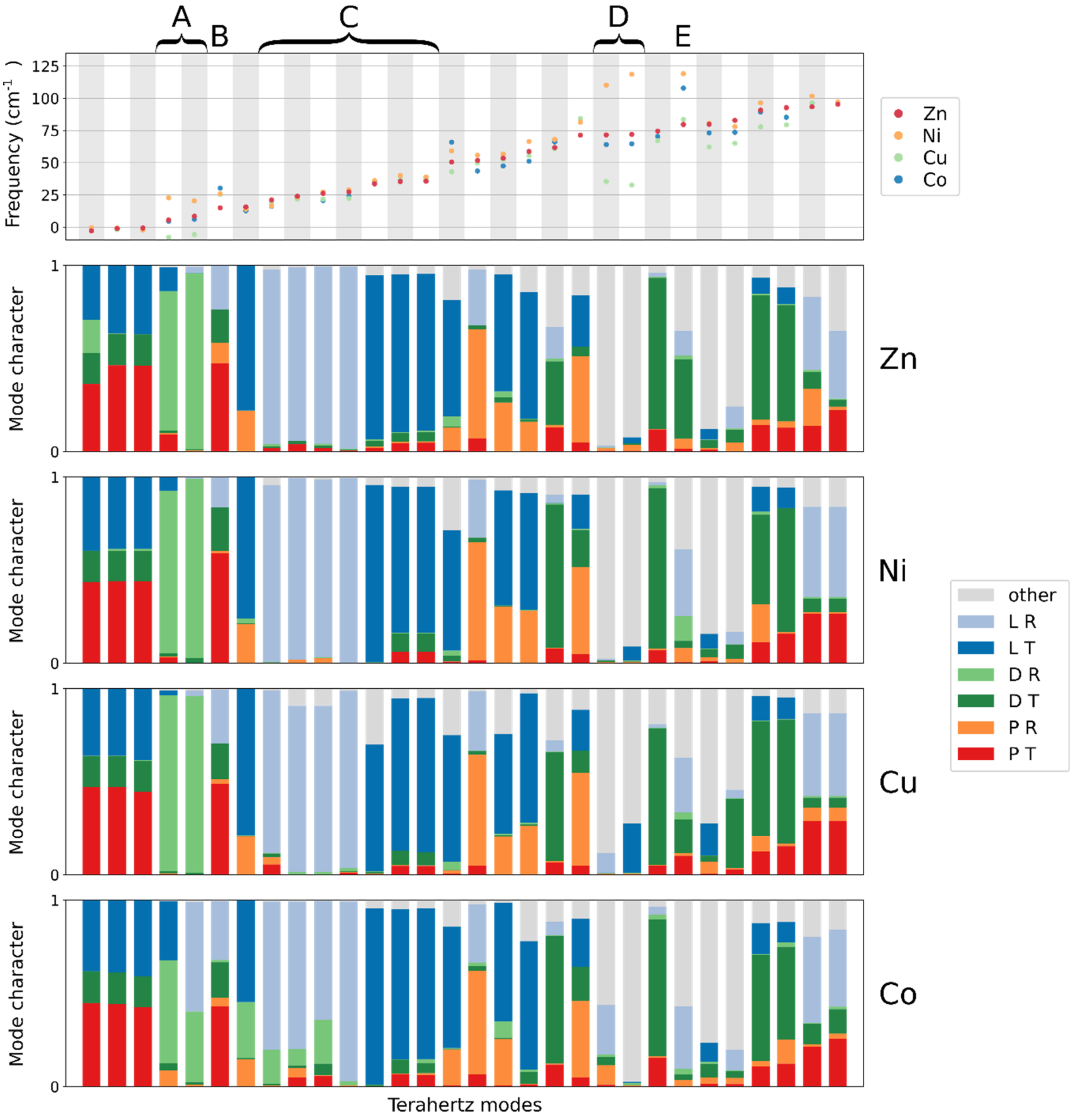

Figure S29: Characterisation of the 30 normal modes with the lowest frequencies of DUT-8(M) (M = Zn, Ni, Cu, Co) materials in their *op* phase. (Top panel) Vibrational frequencies of the different terahertz vibrations. (Bottom panels) Subdivision of the displacements within each terahertz mode in translations (T) and rotations (R) of the 2,6-ndc linker (L), the dabco linker (D), the paddle wheel unit (P), and other types of motions. The normal modes discussed in Section 3.1 are labeled at the top of the figure.

5.2. Closed pore phases

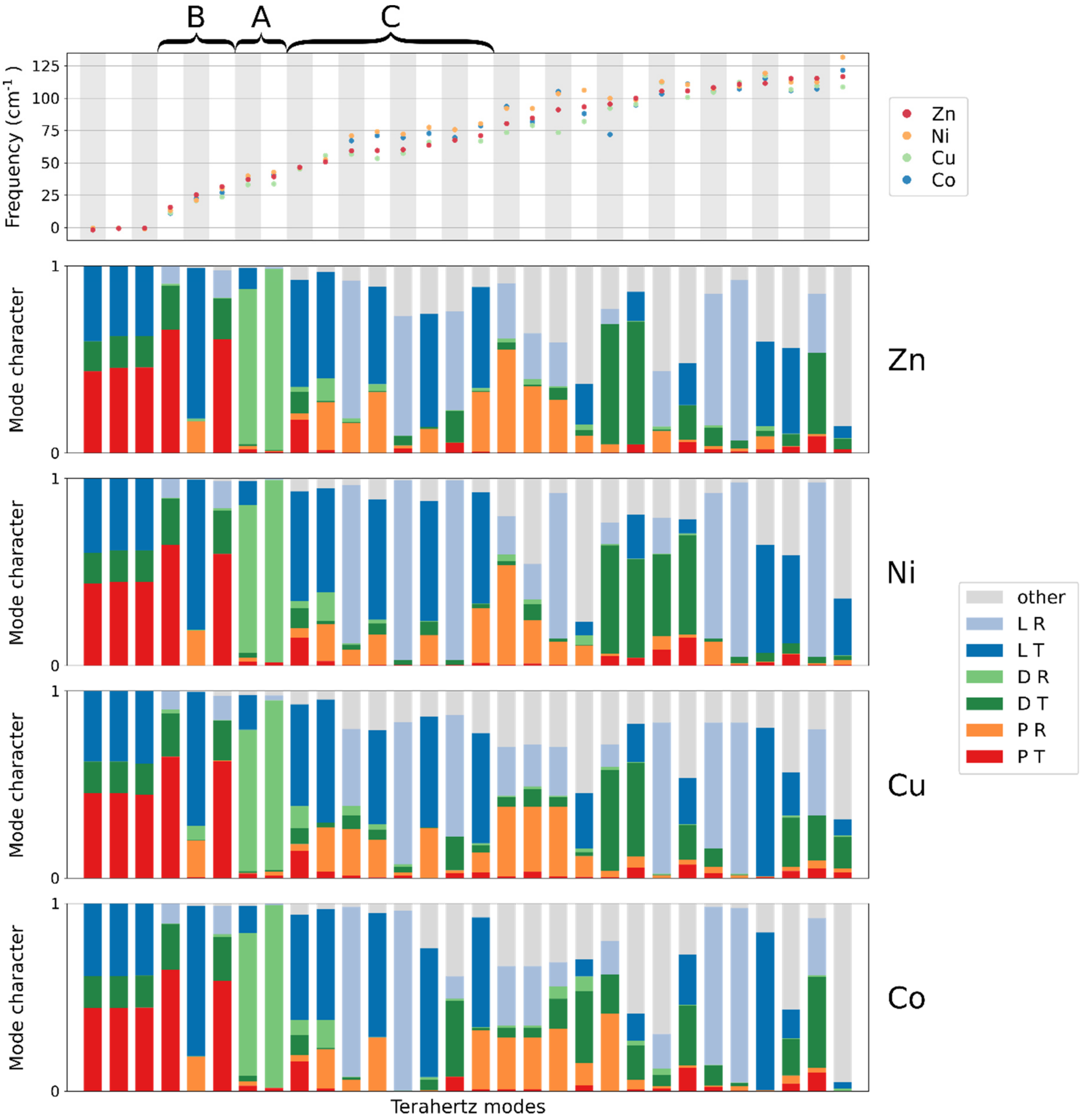

Figure S30: Characterisation of the 30 normal modes with the lowest frequencies of DUT-8(M) (M = Zn, Ni, Cu, Co) materials in their *cp* phase. (Top panel) Vibrational frequencies of the different terahertz vibrations. (Bottom panels) Subdivision of the displacements within each terahertz mode in translations (T) and rotations (R) of the 2,6-ndc linker (L), the dabco linker (D), the paddle wheel unit (P), and other types of motions. The normal modes discussed in Section 3.2 are labeled at the top of the figure.

6. Theoretical DUT-8(M) structures with disintegrated paddle wheel unit

6.1. Optimisation of the structures

To determine the electronic energy differences between the *cp* phase structures with an intact and disintegrated paddle wheel unit reported in Table S3, equilibrium structures with disintegrated paddle wheel units have to be determined. For DUT-8(Zn) this equilibrium structure was obtained by reducing the unit cell volume to very small values and optimising the structure via a fixed volume optimisation. Due to unfavorable repulsive forces between opposite 2,6-ndc linkers in this dense structure, the 2,6-ndc linkers reorganise themselves to counteract this by spontaneously breaking Zn-O bonds allowing these linkers to rotate more easily and increase the dispersion interactions. Once this optimised DUT-8(Zn) structure with disintegrated paddle wheel unit and low unit cell volume has been created, a new Rose-Vinet fit was constructed to determine the optimal unit cell volume and a final fixed volume optimisation was performed. The obtained equilibrium structure is presented in Figure S31. The *cp* phase structures of the other DUT-8(M) materials with disintegrated paddle wheel units were optimised in the same way, but the disintegrated DUT-8(Zn) structure served as the initial structure.

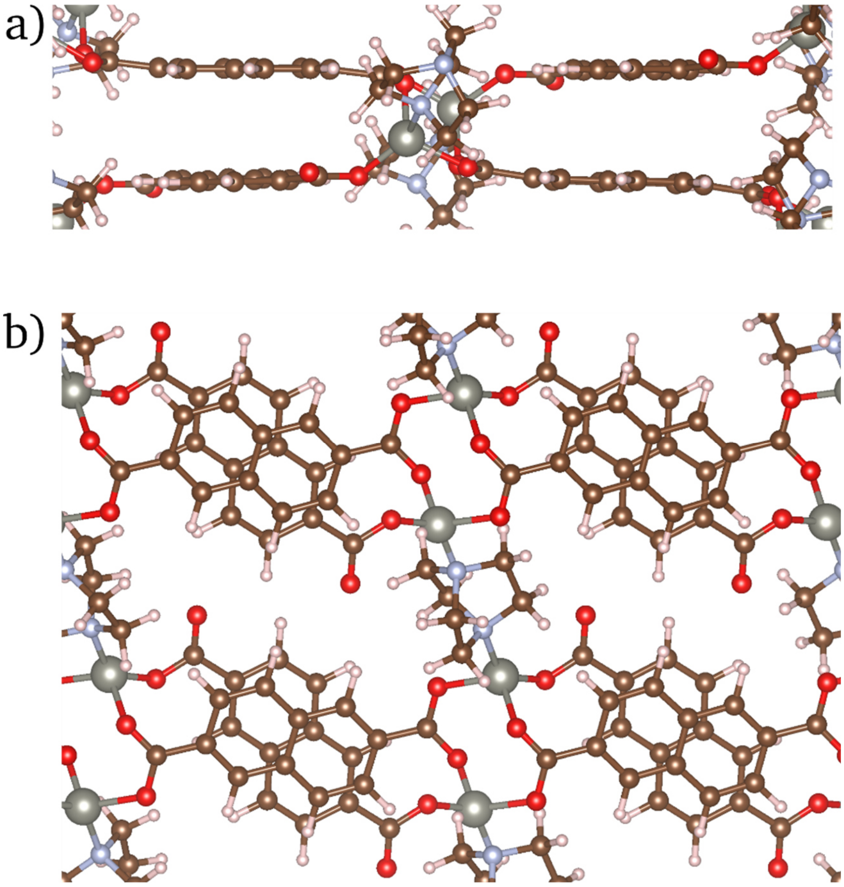

Figure S31: Visualisation of the theoretically optimised *cp* phase structure of DUT-8(Zn) with disintegrated paddle wheel unit. (a) View on the 1D chain with dabco pillars and paddle wheel unit and the linker stacking. (b) View on the pore.

6.2. Terahertz vibrations

Table S4: 11 terahertz vibrations with the lowest frequencies of the *cp* phase of DUT-8(Zn) with intact and disintegrated paddle wheel units. The vibrational frequencies of the two structures are presented together with the frequency difference between both (in cm^{-1}).

	intact	disintegrated	
	wavenumber (cm^{-1})	wavenumber (cm^{-1})	$\Delta_{\text{dis-int}}$ (cm^{-1})
mode 4	15.7	16.2	+0.5
mode 5	25.3	15.9	-9.4
mode 6	31.7	33.3	+1.6
mode 7	37.2	22.8	-14.4
mode 8	39.4	25.0	-14.4
mode 9	46.7	36.3	-10.4
mode 10	50.8	40.4	-10.4
mode 11	59.4	43.5	-15.9
mode 12	59.6	49.0	-10.6
mode 13	60.3	51.8	-8.5
mode 14	63.7	51.5	-12.2

7. Raman active modes in DUT-8(Ni)

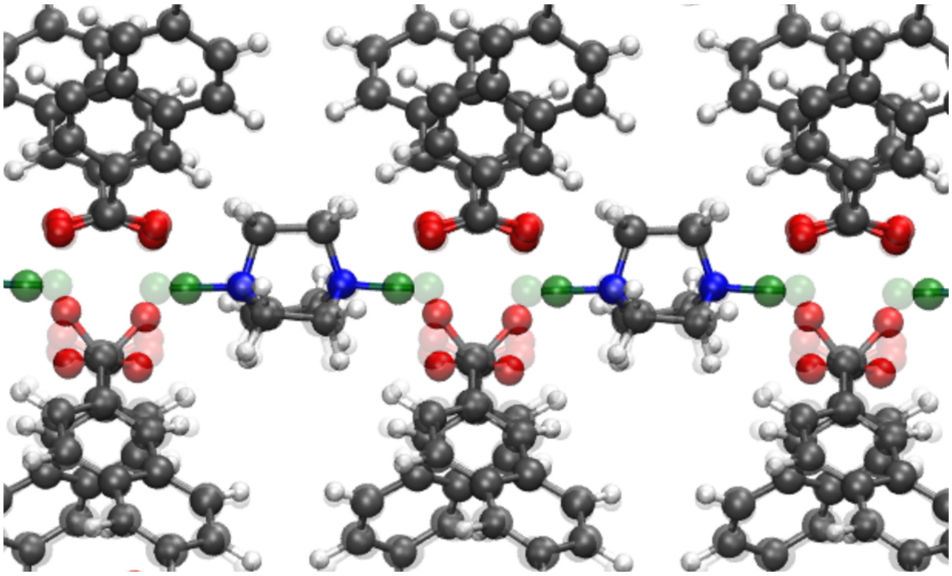

Figure S32: Raman active vibration at 196 cm^{-1} in the *op* phase structure of DUT-8(Ni) inducing stretching of the Ni-N bond.

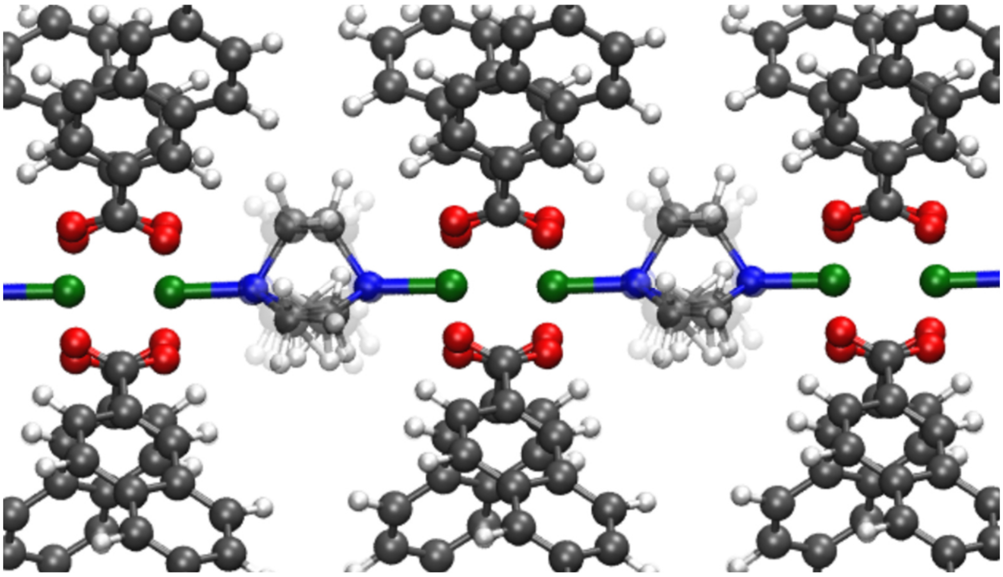

Figure S33: Raman active vibration at 977 cm^{-1} in the *op* phase structure of DUT-8(Ni) inducing stretching of the C-C bonds in the dabco pillar.

8. Intact paddle wheel structures of DUT-8(M) materials

8.1. Open pore phases

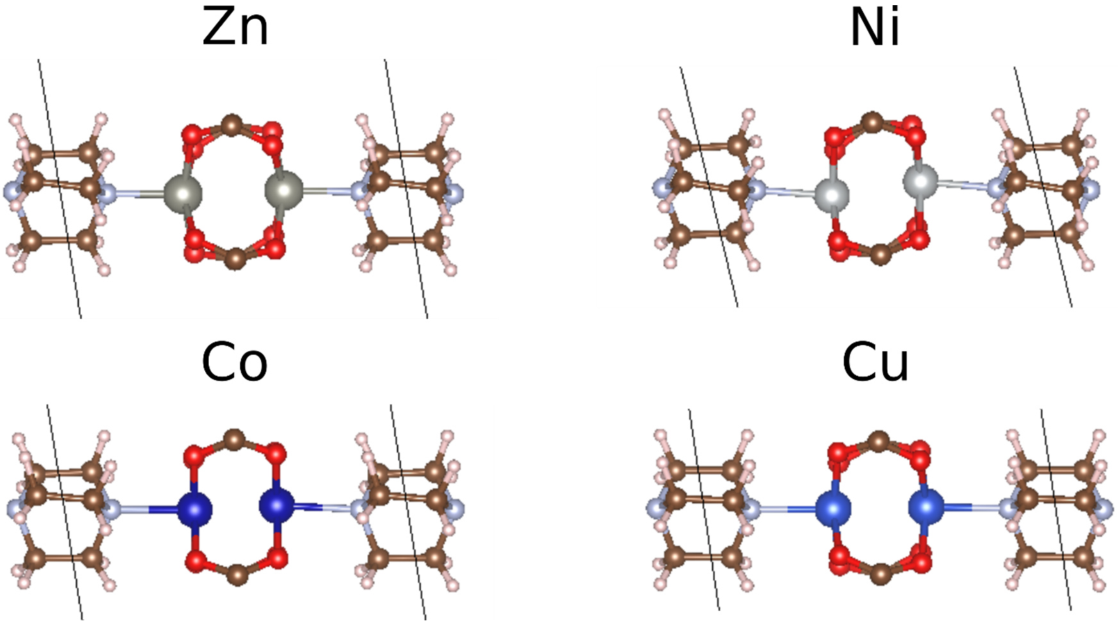

Figure S34: Visualisation of the paddle wheel unit of the theoretically optimised *op* phase structures of DUT-8(M) (M = Zn, Ni, Co, Cu) materials.

8.2. Closed pore phases

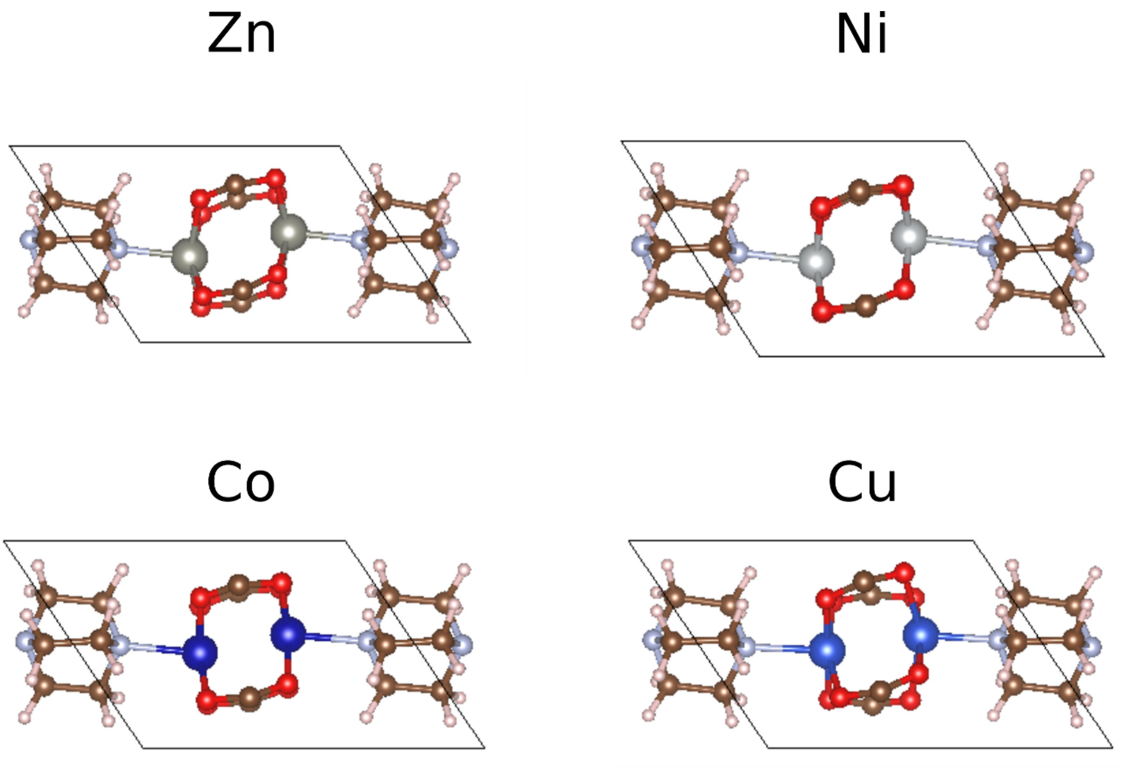

Figure S35: Visualisation of the paddle wheel unit of the theoretically optimised *cp* phase structures of DUT-8(M) (M = Zn, Ni, Co, Cu) materials.

9. Consideration of anharmonicities

As the performed phonon calculations rely on the harmonic approximation, the predicted frequencies may indeed be affected by anharmonicities. These can be taken into account by also considering third- and higher-order derivatives of the energy with respect to the atom displacements. However, this significantly increases the computational cost, which becomes unfeasible for the studied DUT-8 systems. To estimate the anharmonicity of the phonon modes, we have instead calculated their anharmonic frequencies in an approximate way for the op and cp phases of DUT-8(Ni). For each of the 30 phonon modes with the lowest frequencies, we have distorted the equilibrium structure along the harmonically predicted phonon mode by 5 positive and 5 negative displacement amplitudes and calculated the corresponding energy. Afterwards, a 7^{th} order polynomial fit was determined for the potential energy along this specific phonon mode. Subsequently, the Schrödinger equation of the phonon mode was solved numerically and the anharmonic frequency was identified as the energy difference between the two lowest eigenstates divided by Planck's constant. In this way, the anharmonic frequency of a harmonic phonon mode can be determined. Although, this approach neglects the possibility of phonon coupling. For the op phase of DUT-8(Ni), the resulting anharmonic frequencies are compared with the harmonic ones in Figure S36. The latter figure also illustrates the two first eigenstates of the Schrödinger equation of two specific modes.

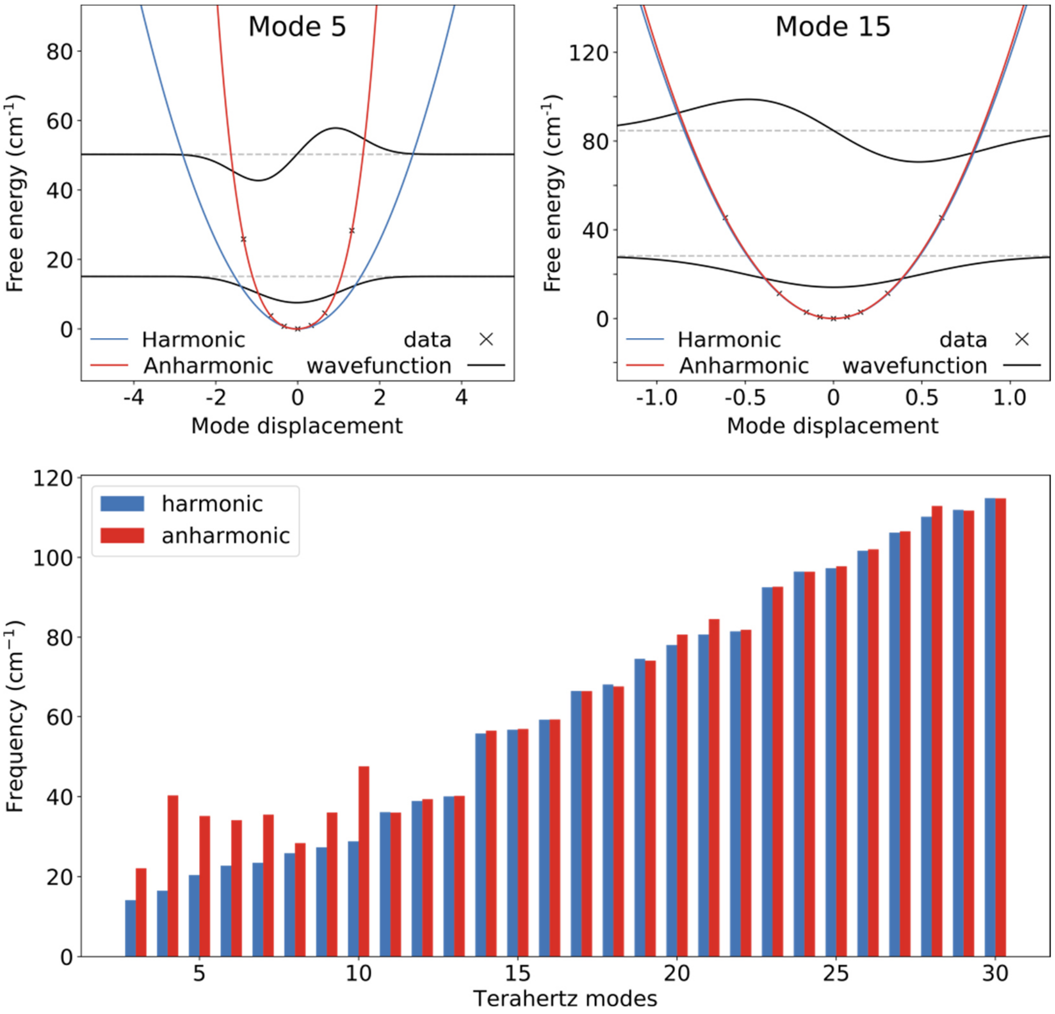

Figure S36. Comparison of the harmonic and anharmonic frequencies of the 30 phonon modes with the lowest frequencies for the op phase of DUT-8(Ni). For modes 5 and 15 the harmonic free energy is compared with the anharmonic free energy and its corresponding eigenstates.

The 3 modes inducing translations of the complete structure (modes 0 to 2) have not been considered. For the phonon modes with the lowest frequencies (modes 3 to 10), the largest differences between the harmonic and anharmonic frequencies can be observed. These modes either involve dabco rotations (modes 3 and 4), a combination of paddle-wheel translations and linker rotations (mode 5), a combination of linker translations and paddle-wheel rotations (mode 6), or rotations of the 2,6-ndc linker (modes 7 to 10). These modes are thus highly anharmonic in the op phase. Interestingely, the anharmonic frequency of these modes is higher than the harmonic one making them less soft. For the phonon modes with higher frequencies, there is only a low level of anharmonicity as shown by anharmonic frequencies which are almost identical to the harmonic ones. Similarly for the cp phase of DUT-8(Ni), the harmonic and anharmonic frequencies of the low-frequency phonon modes are compared in Figure S37.

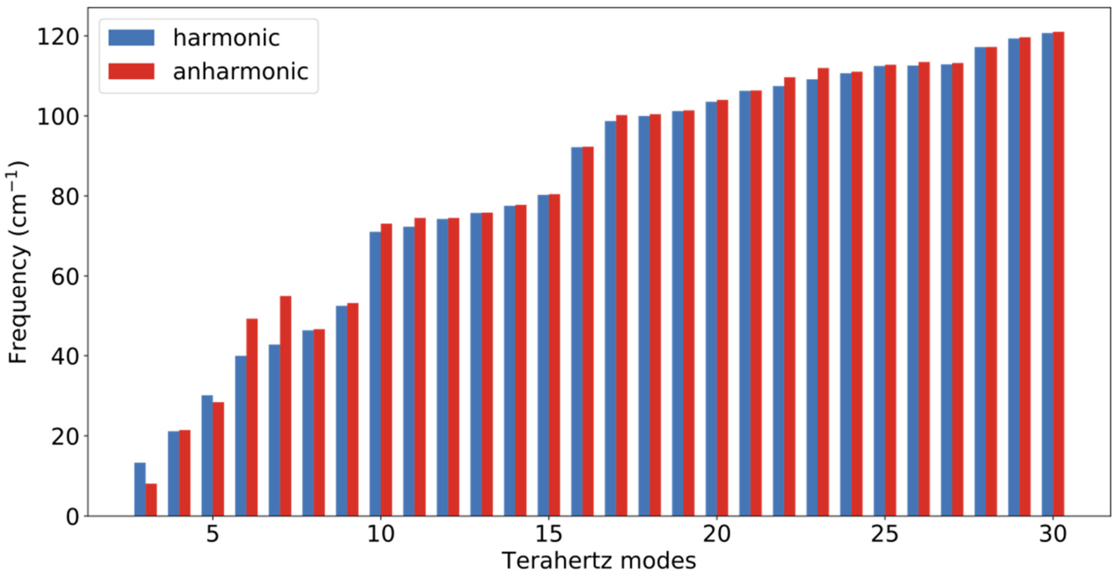

Figure S37. Comparison of the harmonic and anharmonic frequencies of the 30 phonon modes with the lowest frequencies for the cp phase of DUT-8(Ni).

For the cp phase, there are only three phonon modes exhibiting slight anharmonicity. The phonon mode with the lowest frequency inducing a combination of paddle-wheel translations and linker rotations (mode 3) has an anharmonic frequency that is lower than the harmonic one, making it softer. The phonon modes inducing dabco rotations (modes 6 and 7) have an anharmonic frequency which is higher than the harmonic one, similar to what was observed in the op phase.